Acta Materialia 213 (2021) 116963

Contents lists available at ScienceDirect

Acta Materialia

journal homepage: www.elsevier.com/locate/actamat

Full length article

Shear fracture in bulk metallic glass composites

Devashish Rajpoot[a,b], R. Lakshmi Narayan[c,*], Long Zhang[d,*], Punit Kumar[b], Haifeng Zhang[d], Parag Tandaiya[a,*], Upadrasta Ramamurty[b,e]

[a] Department of Mechanical Engineering, Indian Institute of Technology Bombay, Powai, Mumbai 400076, India
[b] Department of Mechanical and Aerospace Engineering in Nanyang Technological University, Singapore 637331, Republic of Singapore
[c] Department of Materials Science and Engineering, Indian Institute of Technology Delhi, Hauz Khas, New Delhi 110016, India
[d] Shi-changxu Innovation Center for Advanced Materials, Institute of Metal Research, Chinese Academy of Sciences, Shenyang 110016, China
[e] Institute of Materials Research and Engineering, Agency for Science, Technology and Research (A *STAR), Singapore 138634, Republic of Singapore

ARTICLE INFO

Article history:
Received 5 March 2021
Revised 12 April 2021
Accepted 2 May 2021
Available online 9 May 2021

Keywords:
Bulk metallic glass composites
Fracture
Martensitic transformation
Shear bands
Plastic deformation

ABSTRACT

Fracture behavior of bulk metallic glass matrix composites (BMGCs) with both transforming and non-transforming β-Ti dendrites under shear and opening modes was examined. Experimental results show that the fracture toughness of all three BMGCs is considerably lower in mode II than in mode I, due primarily to the shear dominant stress state in the former, which renders easy shear band initiation. However, stable crack growth in mode I is insignificant whereas it is considerable in mode II. The toughness of BMGCs reinforced with coarse but non-transforming dendrites in both the modes is higher than the respective values in BMGCs with transforming β-Ti inspite of their ability to strain harden and hence enhanced ductility. Fracture surface features and shear band patterns at notch tips of both mode I and mode II specimens indicate that despite the interactions of dendrites with the shear bands, the fracture criterion and mechanism of BMGCs is identical to that in BMGs. The differences in the fracture behaviour of these BMGCs is rationalized by considering the effect of relaxation enthalpy of the amorphous matrices in addition to the length scale and transforming tendency of the dendrites on the transformation of a shear band into a crack. Implications of these results in terms improving the fracture toughness of BMGCs with transforming dendrites is discussed.

1. Introduction

The lack of ductility in bulk metallic glasses (BMGs), when tested on macroscopic specimens and at temperatures much lower than their glass transition temperature, T_g, is due to the fact that plastic deformation in them manifests in the form of shear bands which, in the absence of an interacting microstructure or stress concentrators, propagate unhindered and lead to failure [1–8]. In an endeavour to improve BMGs' ductility, the composite approach is adopted, wherein a 'microstructure' is introduced in the BMG matrix [1,9–22]. This microstructure typically consists of some reinforcing phase, which are either incorporated via phase partitioning during solidification from the melt [15,16,19,22,23] or infiltrated by extrinsic means in the melt [12,20,21,24]. Of the different types of BMG matrix composites (BMGCs), the ones reinforced with *in situ* precipitated crystalline β-Ti dendritic phases appear the most promising. The β-Ti dendrites are softer than the amorphous matrix, which results in BMGCs with lower yield strength [25–27]. The size, volume fraction and interdendritic spacing of the β-Ti dendrites can be optimized so as to tailor strength - elongation to failure combinations [15,16,19,28,29]. Importantly, these BMGCs possess exceptional mode I fracture toughness, K_{Ic} [30,31], which is the only mode that all the fracture studies in BMGCs reported hitherto were performed in. This leads us to identify the following critical issues pertaining to the fracture behavior of BMGCs.

- Prior fracture studies on monolithic bulk metallic glasses (BMGs) show that crack initiation is relatively easier in shear-dominant loading conditions (modes II and III), with the mode II fracture toughness, K_{IIc}, of a Zr-based BMG being only about one-fourth of K_{Ic} [32–39], which was attributed to shear bands require considerably smaller far field stress to initiate in these loading conditions [33,37,40,41]. Whether K_{IIc} of BMGCs will be lower or higher than K_{Ic} is yet to be ascertained.
- During the design of BMGCs, an implicit assumption that ductility directly scales with the fracture toughness, and there-

---

[*] Corresponding authors.
E-mail addresses: rlnarayan@mse.iitd.ac.in (R.L. Narayan), zhanglong@imr.ac.cn (L. Zhang), parag.ut@iitb.ac.in (P. Tandaiya).

https://doi.org/10.1016/j.actamat.2021.116963
1359-6454/

fore enhancing the ductility automatically leads to materials with higher toughness, is made. Consequently, significant efforts are directed towards ductility improvement of BMGCs by varying the composition of dendrites and invoking different strain hardening mechanisms in them. For instance, Zhang et al. [16] have shown that compositional modifications of β-Ti dendrites lead to deformation induced martensitic transformations in them and improves their shear band arresting capabilities. Such transformation induced plasticity (TRIP) effects can be combined with microstructural optimization to obtain a BMGC that is simultaneously strong and ductile [16,18,42–46]. While the ductility-fracture toughness scaling may indeed be true in crystalline alloys, no such connection in BMGs. (For example, many BMGs exhibit high fracture initiation toughness values despite breaking immediately after macroscopic yielding in uniaxial tension [1,32,47–49].) In light of this, if the efforts to improve the ductility of BMGCs will automatically lead to enhanced fracture toughness requires experimental verification. In a similar vein, it is also not clear as to what role the TRIP induced strain hardening will have on fracture toughness.

- It is widely known that the structural state of the BMG has a direct bearing on its ability for shear band mediated plasticity, and, in turn, on the fracture toughness. For example, Narayan et al. [50] have established that BMGs that form more shear bands ahead of its notch tip are tougher, which was later reaffirmed by Shao et al. [51]. Since dendrites in BMGCs not only resist the propagation of shear bands, but also can act as their nucleators, it is unknown as to how the combination of all these factors—that too under the triaxial state of stress that prevails at the notch tip—will influence the toughness of BMGCs.
- With respect to the crack propagation in BMGCs, Launey et al. [30] have shown that some Zr-based BMGCs exhibit increasing fracture resistance (R-curve behaviour) in mode I with increasing crack length. However, it has not yet been determined if the same fracture resistance behaviour is observed under mode II loading conditions. Moreover, the degree of fracture resistance and the extent to which stable crack growth occurs in a mode I BMGC fracture specimen depends on the volume fraction of dendrites and the interdendritic spacing. It is then worth asking if, besides these parameters, the transforming nature of β-Ti dendrites will also lead to a greater degree of fracture resistance.

With the motivation to address all the above-mentioned issues, mode I and mode II fracture experiments are conducted on three notched Zr/Ti-based BMGCs in this study. Of these, one contains stable β-Ti dendrites whereas the other two contain metastable β-Ti dendrites, which undergo deformation induced transformation. The microstructures of these BMGCs are optimized for obtaining good ductility and strength. Nevertheless, apart from subtle differences, the dendrites sizes and volume fractions in all BMGC are broadly similar. Results indicate that mode I fracture initiates at higher loads for BMGC that contain stable β-Ti dendrites compared to that in the other two BMGCs. Alternately, mode II fracture toughness is relatively higher for the BMGC that has finer metastable β-Ti dendrites. It is also noted that all the mode II BMGC specimens exhibit fracture resistance with increasing crack length. However, the rate of increase in fracture resistance and the load at which fracture finally occurs is highest for the stable β-Ti dendrite reinforced BMGC. To rationalize these results, the crack-microstructure interactions in mode I and mode II specimens are studied in detail. Finally, the relative influence of microstructural parameters, dendrite metastability and the structural state of the matrix on mode I and mode II fracture behaviour of the three BMGCs is discussed.

2. Materials and experiments

2.1. Materials and microstructural characterization

Three in situ dendrite reinforced BMGCs, with the compositions of $Zr_{39.6}Ti_{33.9}Cu_{6.4}Nb_{7.6}Be_{12.5}$, $Ti_{45.7}Zr_{33}Cu_{5.8}Ni_{3}Be_{12.5}$, and $Ti_{41.8}Zr_{33.5}Cu_{6.9}Co_{1.2}Be_{16.6}$ (at.%) are examined in this study. All the three are prepared by arc melting in the form of cylindrical bar with the cross-section dimension of 12 mm * 5 mm. The processing details of these alloys can be found elsewhere [17]. These compositions were specifically chosen as they exhibit the most optimum combination of strength and elongation to failure [16,19,28]. Small cubes of size 4 mm × 4 mm × 4 mm are sectioned from each BMGC using wire cut electrical discharge machining (EDM). These cubes are mounted and mechanically polished to a mirror-like surface finish for microstructural observations. Microstructural examination is conducted using a field emission scanning electron microscope (FESEM, JEOL 7600) in the back-scattered electron (BSE) mode and the field emission transmission electron microscopy (TEM, Talos F200X). Compositions of different phases are measured using the Energy-dispersive X-ray spectroscopy (EDS) feature of the FESEM. Additional small pieces are sectioned from these bars to perform differential scanning calorimetry (Netzsch DSC 204F1). The heating and cooling rate employed for DSC measurements is 20°C/minute.

2.2. Material nomenclature

For ease of reference, each alloy is labelled on the basis of their microstructural characteristics. Representative microstructures of the three as cast BMGCs, $Zr_{39.6}Ti_{33.9}Cu_{6.4}Nb_{7.6}Be_{12.5}$, $Ti_{45.7}Zr_{33}Cu_{5.8}Ni_{3}Be_{12.5}$, and $Ti_{41.8}Zr_{33.5}Cu_{6.9}Co_{1.2}Be_{16.6}$, are shown in Fig. 1 (a)-(c). Each alloy contains a dendritic phase embedded within a featureless matrix. Fig. 1 (d) shows the XRD scans obtained from the three BMGCs. The angular positions of diffraction peaks and broad humps, which correspond to a body-centred cubic (bcc) phase and an amorphous phase, respectively, in all BMGCs are identical. From this, it is inferred that the dendrites are a crystalline phase; the micrographs show that they are uniformly dispersed in the amorphous matrix. While the details of the phase compositions in each alloy will be presented later, measurements confirmed that the dendrites of $Zr_{39.6}Ti_{33.9}Cu_{6.4}Nb_{7.6}Be_{12.5}$ and $Ti_{41.8}Zr_{33.5}Cu_{6.9}Co_{1.2}Be_{16.6}$ are coarser than those of $Ti_{45.7}Zr_{33}Cu_{5.8}Ni_{3}Be_{12.5}$. Therefore, the latter will be referred to as ‘FD’ (fine dendrites) in keeping with the smaller size of the dendrites. The other two BMGCs examined in this work are referred to as ‘CD’, which stands for ‘coarse dendrites’. In addition, the nomenclature also contains a reference to the tendency of the dendrites to undergo stress induced transformation. The letters ‘T’ and ‘NT’ are used for referring to BMGCs containing transforming and non-transforming dendrites, respectively. On this basis, $Zr_{39.6}Ti_{33.9}Cu_{6.4}Nb_{7.6}Be_{12.5}$, which contains non-transforming dendrites, will hitherto be referred to as CD-NT. Since $Ti_{41.8}Zr_{33.5}Cu_{6.9}Co_{1.2}Be_{16.6}$ and $Ti_{45.7}Zr_{33}Cu_{5.8}Ni_{3}Be_{12.5}$ contain transforming dendrites, they will henceforth be referred to as CD-T and FD-T, respectively.

2.3. Tension tests

Tensile specimens with dimensions, 6 mm × 2 mm × 0.6 mm (length × width × thickness), are sectioned from the bars of the three BMGCs via wire-cut EDM. These specimens are polished on both sides to a mirror finish. Uniaxial tension tests are performed on ZwickRoell micro-tensile testing machine at a nominal strain rate of 10^{-3} s^{-1}. Displacement is measured via a laser extensometer, which has a resolution of 120 pixel per mm. The side surfaces

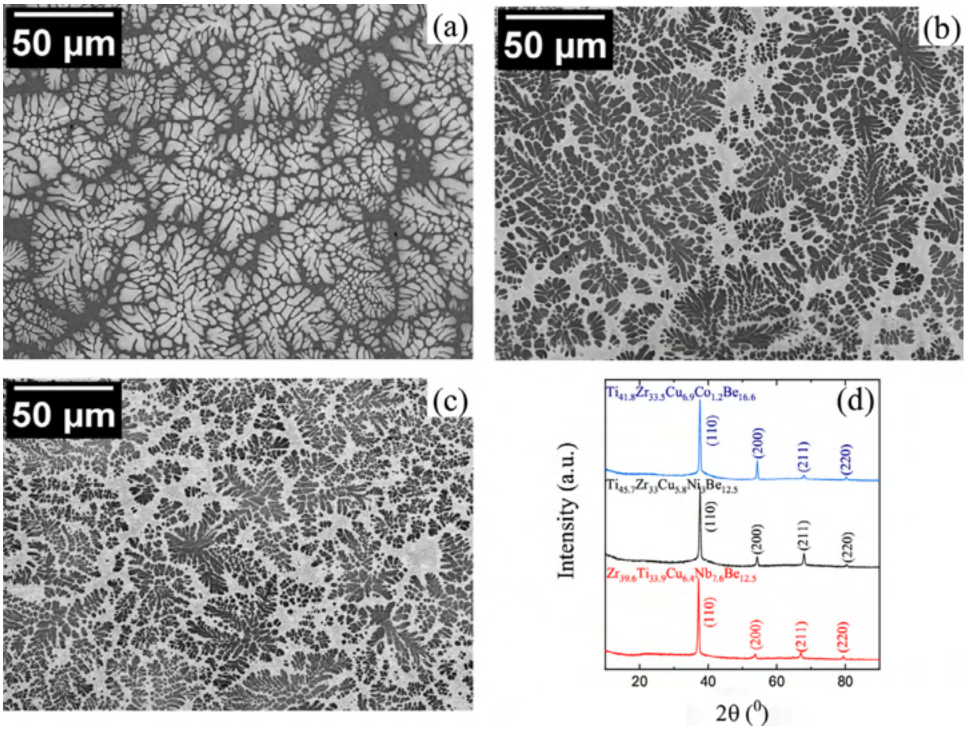

Fig. 1. Representative microstructures of in situ BMGCs (a) $Zr_{39.6}Ti_{33.9}Cu_{6.4}Nb_{7.6}Be_{12.5}$ (CD-NT), (b) $Ti_{45.7}Zr_{33}Cu_{5.8}Ni_{3}Be_{12.5}$ (FD-T), (c) $Ti_{41.8}Zr_{33.5}Cu_{6.9}Co_{1.2}$ $Be_{16.6}$ (CD-T), and (d) their XRD scans.

and fracture surfaces of the tensile-tested specimens are examined in the SEM and small portions near the failure sites are extracted through focused ion beam (FIB) machining and observed inside the TEM.

2.4. Fracture experiments

Symmetric and asymmetric four-point bend specimens are extracted using wire-cut EDM from the three BMGC bars for conducting pure mode I and mode II fracture experiments, respectively. Schematic illustrations of these specimens are shown in Fig. 2. The symmetric four-point bend (S4PB) specimen has length (L) and width (w) of 30 mm and 5 mm, respectively, whereas the thickness (t) is 3.5 mm. While the width and thickness of the asymmetric four-point bend (AS4PB) specimens are the same as that of S4PB specimens, their L is 40 mm. Notches that are 2.5 mm deep are introduced in both types of specimens using wire-cut EDM at the indicated locations in Fig. 2. The diameter of the notch root obtained is ~100 μm. Two Berkovich indents are made to mark the locations on the notch profile that are above and below the centre of curvature of the notch, using an instrumented nanoindenter.

Fracture tests are performed on a universal testing machine (UTM) under a constant cross head speed of 0.002 mm/s. For these tests, four-point bend test fixtures that have 3 mm diameter rollers at the load point area are attached to the UTM. Near the load point area, grooves are made in the specimens to avoid stress concentrations and to provide intimate contact between the specimen and loading pins. Before testing, specimen surfaces are polished to a mirror finish. A long-distance optical microscope with a 60X magnification capacity and an Olympus DP22 CCD high-resolution camera attached is used to investigate the deformation of the notch root in real time. Videos at 10 frames per second are recorded to monitor the rotation angle and crack sliding displacement. The computer connected to the UTM and long-distance optical microscope are synchronized to obtain the loads corresponding to rotation angles and crack sliding displacements. The indents made on both sides of the notch are used as a reference to measure the crack opening (δ_O) and crack sliding displacements (δ_S). For every alloy composition two tests are performed each in mode I and mode II loading conditions.

One sample of each case considered above is unloaded at different stages of loading for observing the near-tip region under a high-resolution optical microscope and SEM. After the specimens are broken, their fracture surfaces and side surfaces are examined in SEM and TEM to understand the operative failure mechanisms.

2.5. Estimation of energy release rate

The energy release rate, J_I, of the fracture specimen in mode-I loading conditions is calculated from [52–54],

$$J_I = \frac{\eta_I}{Bb}\int_0^{\theta} M d\theta \tag{1}$$

where η_I is a geometric factor that depends on specimen dimensions, B is the thickness of the specimen, b is ligament length, M is the moment acting on the notch plane, and θ is the total specimen rotation at the notch plane. M at the notch plane is calculated using the relation,

$$M = \frac{P}{2}(L_1 - L_2) \tag{2}$$

where P is load, L_1 and L_2 are the distances of the lower and upper left loading pins from the notch, respectively. θ is measured from the video recordings of the test using the ImageJ software. The incremental area under the M-θ curve is calculated for every 100 N increment in P using the trapezoidal rule in the Matlab R2019a software.

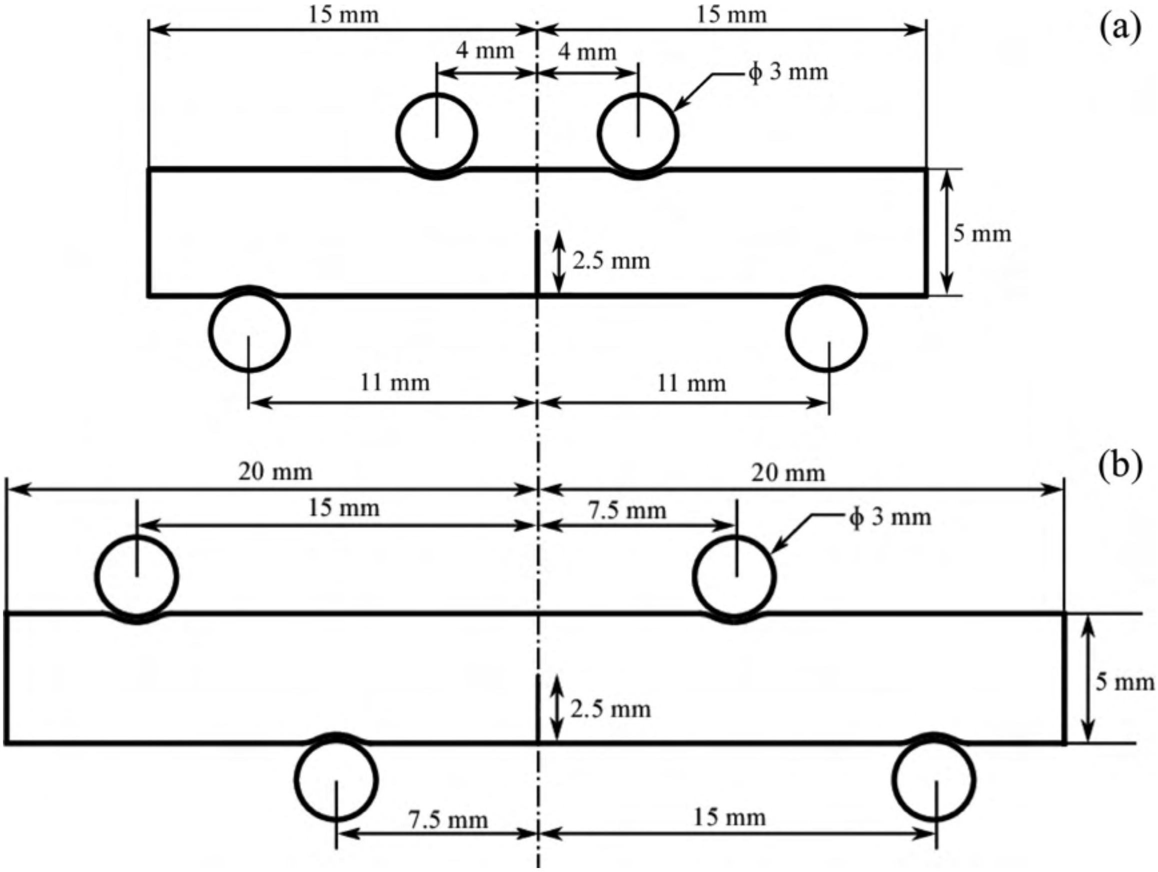

Fig. 2. Schematic drawings of (a) symmetric four-point bend and (b) asymmetric four-point bend specimens used for mode I and mode II fracture experiments on BMGCs.

Similarly, the energy release rate, J_{II}, of fracture specimen in mode-II is calculated from [52–54],

$$J_{\mathrm{II}} = \frac{\eta_{\mathrm{II}}}{Bb} \int_{0}^{\delta_s} V \mathrm{d}\delta_s \tag{3}$$

where η_{II} is a geometric factor, V is the shear force acting on the notch plane, and δ_s is notch sliding displacement. Shear force at the notch plane is calculated using the relation,

$$V = \frac{P}{2} \times \frac{(L_3 - L_4)}{(L_3 + L_4)} \tag{4}$$

where L_3 and L_4 are the distances of the upper left loading pin and lower left loading pin from the notch, respectively. The incremental area under the V-δ_s curve is measured for every 100 N increment in P. The values of η_{I} and η_{II} are 2 and 1, respectively [54].

3. Results

3.1. Microstructural characterization and mechanical properties

Figs. S1 to S3 display the EDS scans of the three BMGCs. The dendrites in CD-NT are leaner in Nb, whereas the dendrites of FD-T, and CD-T are leaner in all constituents except Ti. These compositional variations result in the difference in contrast of the matrices and dendrites in Fig. 1 (a)-(c) as imaging was performed in the BSE mode. Nevertheless, since the dendritic phases of all compositions have Ti as the dominant constituent, they are referred to as the β-Ti phase. The complete chemical compositions of the dendrites and matrices and the microstructural characteristics, such as volume fraction, V_d, size, Ω, and interdendritic spacing λ, of the former in the three BMGCs are listed in Table 1.

The V_d in CD-NT and FD-T are 55% each, whereas it is 47% in CD-T[1]. Ω and λ of FD-T are 77 ± 13 μm and 59 ± 12.3 μm, respectively, which is 30% lower than those of CD-NT and CD-T.

The DSC traces of the BMGCs are shown in Fig. 3. All the traces exhibit an endothermic event corresponding to the glass transition and a supercooled liquid region, followed by one or two exothermic peaks characteristic of crystallization. The glass transition temperatures, T_g, of CD-NT, FD-T, and CD-T BMGCs are 633 K, 659 K, and 640 K, respectively. Prior to T_g, an exothermic hump is also observed in all the DSC traces. The area under the exothermic humps corresponds to the enthalpy of relaxation, ΔH_{rel}, of the amorphous matrix. ΔH_{rel} is a measure of the energy difference between the ‘as quenched’ and relaxed state of the amorphous phase and is therefore a quantitative measure of its structural state [42,55,56]. A lower magnitude of ΔH_{rel} implies that the structure is relaxed and closer to the equilibrium glass state. In addition to this, the partial transformation of β-Ti to ω-Ti also contributes to the exothermic humps of FD-T and CD-T BMGCs. After deconvoluting the contributions from this transformation, the estimated values of ΔH_{rel} of the matrices of CD-NT, FD-T, and CD-T are 10.44, 6.75, and 8.5 J/g, respectively. Note that these values have also been normalized with respect to the volume fraction of the matrix in each BMGC. This implies that the amorphous matrices in FD-T and CD-T are relatively more relaxed than that in CD-NT.

The engineering stress, σ, vs. engineering strain, ε, responses of the three BMGCs are displayed in Fig. 4 (a). Values of the

---

[1] Owing to precipitation heterogeneity of dendrites, the V_d of these composites exhibit 5-10% variation depending on the location at which it is measured. Since fracture is a highly localized phenomenon, the V_d reported in this work corresponds to that measured near the notch tips of the fracture specimens.

Table 1
The compositions of dendrite and matrix phase of BMGCs with the measured V_d, Ω, and λ of the dendrites.

Material	Chemical composition (wt%)		V_d (%)	Ω (μm)	λ (μm)
	Dendrite	Matrix			
$Zr_{39.6}Ti_{33.9}Cu_{6.4}Nb_{7.6}Be_{12.5}$ (CD-NT)	$Zr_{55.1}Ti_{27.9}Nb_{15.2}Cu_{1.7}$	$Zr_{53.7}Ti_{17.2}Nb_{4.7}Cu_{11.9}Be_{12.5}$	55±0.6	107±16.7	86.6±18.7
$Ti_{45.7}Zr_{33}Cu_{5.8}Ni_3Be_{12.5}$ (FD-T)	$Ti_{47.5}Zr_{49.4}Cu_{2.4}Ni_{0.7}$	$Ti_{25.8}Zr_{46.8}Cu_{9.7}Ni_{5.2}Be_{12.5}$	55±0.7	77±13	59±12.3
$Ti_{41.8}Zr_{33.5}Cu_{6.9}Co_{1.2}Be_{16.6}$ (CD-T)	$Ti_{44.6}Zr_{50.5}Cu_{2.9}Co_{0.4}$	$Ti_{24.2}Zr_{47.1}Cu_{10.4}Co_{1.7}Be_{16.6}$	47±1.3	101±15	89.3±19.4

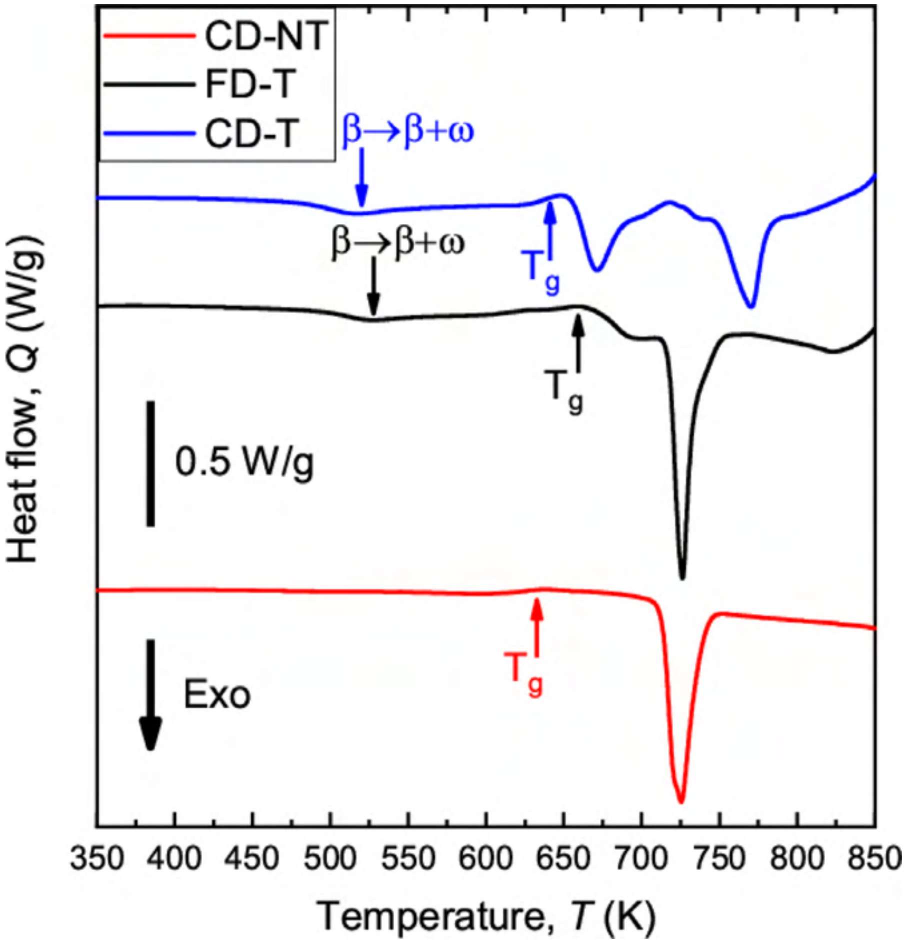

Fig. 3. DSC scans obtained on the as cast $Zr_{39.6}Ti_{33.9}Cu_{6.4}Nb_{7.6}Be_{12.5}$ (CD-NT), $Ti_{45.7}Zr_{33}Cu_{5.8}Ni_3Be_{12.5}$ (FD-T), and $Ti_{41.8}Zr_{33.5}Cu_{6.9}Co_{1.2}$ $Be_{16.6}$(CD-T) bulk metallic glass composites.

Table 2
Summary of the mechanical properties of BMGCs.

Material	E (GPa)	ν	YS (MPa)	UTS (MPa)	ϵ_u (%)	ϵ_f (%)
$Zr_{39.6}Ti_{33.9}Cu_{6.4}Nb_{7.6}Be_{12.5}$ (CD-NT)	98.8 ±0.6	0.366	1036.5 ±12.4	1170.1 ±14.8	4.5 ±0.4	9.7 ±2.2
$Ti_{45.7}Zr_{33}Cu_{5.8}Ni_3Be_{12.5}$ (FD-T)	106.7 ±0.6	0.354	1250.4 ±15.3	1480.4 ±18.6	6.9 ±0.7	8.1 ±1.4
$Ti_{41.8}Zr_{33.5}Cu_{6.9}Co_{1.2}Be_{16.6}$ (CD-T)	107.3 ±0.5	0.354	1069.9 ±19.1	1258.9 ±22.3	3.4 ±0.4	6.4 ±1.1

Young's modulus, E, Poisson's ratio, ν, yield strength, YS, ultimate tensile strength, UTS, uniform elongation, ε_u, and strain-to-failure, ε_f, extracted from the tensile stress-strain responses are listed in Table 2. While E of the three composites is similar, there are significant differences in the post-yield responses. FD-T has the highest YS of 1250.4 ± 15.3 MPa, whereas YS of CD-NT and CD-T are ~200 MPa lower. Both FD-T and CD-T strain harden significantly to UTS of 1480.4 ± 18.6 MPa and 1258.9 ± 22.3 MPa, respectively. In contrast, CD-NT undergoes moderate hardening and has a UTS of 1170 ± 14 MPa. Nevertheless, CD-NT exhibits highest strain-to-failure, ε_f ~9.7%, owing to significant post-necking elongation. While CD-T also exhibits ~2% post-necking elongation, FD-T fails immediately after attaining peak strength. However, FD-T exhibits a greater ε_u ~6.9%, which is twice as high as that of the other two alloys.

To understand the variations in mechanical properties, the side surfaces of the tensile-tested specimens are examined in the SEM. Representative micrographs are displayed in Fig. 4 (b)-(d). Several shear bands with low shear offsets cut across the dendrites and matrix in CD-NT. In contrast, FD-T and CD-T have comparatively fewer shear bands, each of which have larger shear offsets. Some dendrites in these composites appear to have resisted shear band penetration. TEM micrographs of the dendrites in FD-T and CD-T are displayed as insets in Fig. 4 (c) and 4 (d), respectively. These images reveal the presence of several thin elongated martensitic

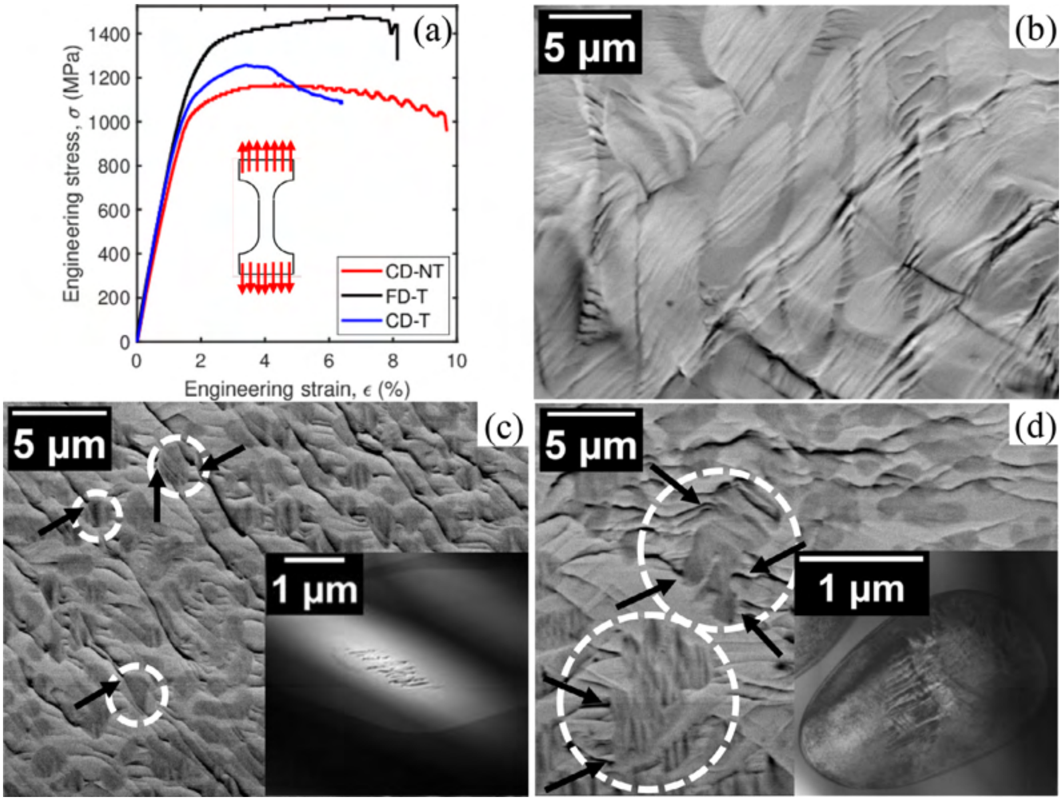

Fig. 4. (a) Tensile stress-strain responses of the three BMGCs examined in this work. Microstructures of the tensile-tested (b) CD-NT, (c) FD-T, and (d) CD-T BMGCs. Insets in (c) and (d) are TEM images of the dendrites in the tensile-tested BMGCs. Arrows highlight the regions where dendrites arrest shear bands.

plates within the dendrites; this phase is identified as the α”-Ti phase.

However, the same phase is not present in the dendrites of tensile-tested CD-NT. Prior studies have reported that β-Ti only undergoes deformation-induced transformation to α”-Ti in its metastable form, which depends on its composition. To account for the constituents that improve the stability of β-Ti, an empirical index, referred to as the Molybdenum equivalent (MoEq), is developed. The form of this index is as follows [57].

$$\begin{aligned}\mathrm{MoEq} = {} & 1.0\,(\mathrm{wt.\%\ of\ Mo}) + 0.67\,(\mathrm{wt.\%\ of\ V}) + 0.28\,(\mathrm{wt.\%\ of\ Nb}) \\ & + 1.43\,(\mathrm{wt.\%\ of\ Co}) + 1.11\,(\mathrm{wt.\%\ of\ Ni}) \\ & + 0.77\,(\mathrm{wt.\%\ of\ Cu}) - 1.0\,(\mathrm{wt.\%\ of\ Al})\end{aligned} \tag{6}$$

The coefficients associated with the wt.% of each constituent is a relative measure of their effectiveness in stabilizing β-Ti. Estimated values of the MoEq of the β-Ti dendrites in CD-NT, FD-T, and CD-T are 5.57, 2.63, and 2.81, respectively. Considerably lower MoEq of the dendrites in FD-T, and CD-T explains their metastability and susceptibility to undergo transformation to α”-Ti upon stressing at 298 K [17,57,58].

Zhang et al. [16] conducted tensile tests on BMGCs reinforced with stable and metastable β-Ti and noted that the improved strain hardening, and hence greater ductility in the latter is a consequence of β to α” transformation. They provided the following rationale for this. Irrespective of the type of β-Ti reinforcements, plastic deformation initiates in the dendrites of the BMGCs as they are softer than the matrix. The plastic deformation in the dendrites and elastic deformation in the matrix are compatible as the latter can accommodate elastic strains up to 2%. However, this strain compatibility breaks down at the matrix-dendrite interface with increasing plastic strain and results in the nucleation of shear bands in the matrix. The propagation of these shear bands is hindered by the dendrites. The extent to which the β-Ti dendrites can arrest shear bands is a function of its strain hardenability. It is discovered that stable β-Ti dendrites, which do not undergo martensitic transformation, deform via planar slip. Since planar slip limits interactions between dislocations, the dendrites do not undergo significant strain hardening. In addition, planar slip in the dendrites, if suitably oriented with respect to the shear band plane, also provides a channel for shear bands to propagate. Since propagation of shear bands hastens shear localization, BMGCs that contain stable β-Ti dendrites, such as CD-NT, undergoes limited work hardening and exhibits low uniform elongation (see Fig. 4 (a)). In contrast, the deformation induced transformation of β-Ti to α”-Ti locally re-orients the slip planes and increases the interactions between dislocations in the dendrites. This, in turn, enhances strain hardening in the dendrites and improves their effectiveness in mitigating shear band propagation. This delays the onset of macroscopic shear localization, enhances overall work hardening of the BMGC and enhances its ductility. The enhanced hardening rates of FD-T and CD-T can be attributed to this mechanism. However, FD-T is significantly more ductile than CD-T. This difference can be attributed to the relatively lower MoEq of the dendrites in the former, which destabilizes β-Ti and promotes more martensitic transformations in it. Therefore, the dendrites of FD-T are expected to be more effective in arresting shear band propagation than those of CD-T and will hence exhibit better ductility [16].

Overall, it is observed that the subtle variations in microstructural length scales and metastability of β-Ti influence the plastic deformation characteristics of the three BMGCs. While the BMGC containing non-transforming dendrites has the highest ε_f, the strain hardening rate and ε_u is higher for the BMGC which contains the highest volume fraction of transforming dendrites. In contrast, variations in Ω and λ does not appear to have a significant effect on mechanical properties, which matches with the conclusions made in prior studies [15,16,19].

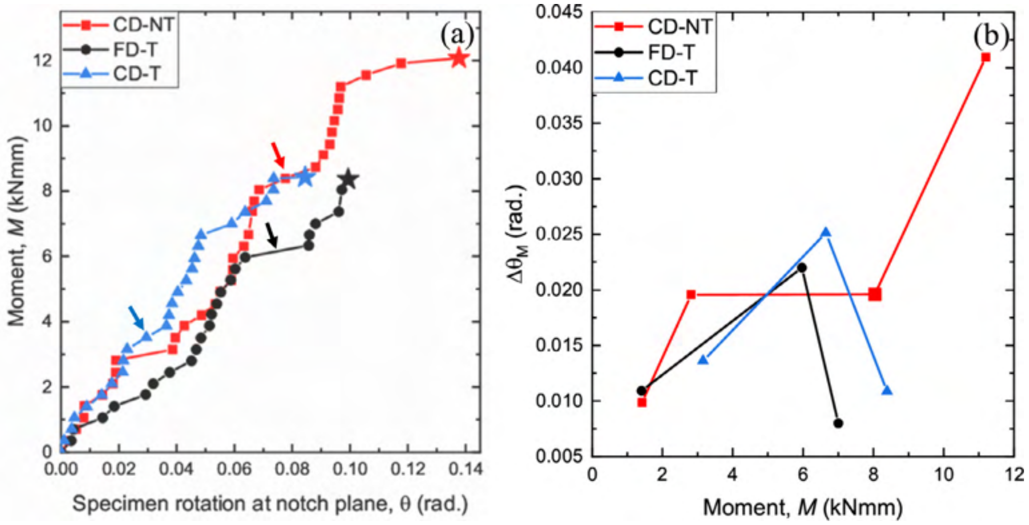

Fig. 5. Variations in (a) Moment, M, with specimen rotation at the notch plane, θ, and (b) magnitude of θ excursions, $\Delta\theta_M$, with M for mode I fracture specimens of the three BMGCs. Arrows in (a) indicate discrete variations in θ.

3.2. Fracture experiments

3.2.1. Energy release rate and notch tip plasticity in mode I fracture experiments

Fig. 5 (a) shows the representative M-θ responses obtained on the notched S4PB (mode I) specimens of the three BMGCs. For each BMGC, although M broadly increases with θ, the variations are not entirely smooth as several intermittent bursts in θ, at constant M, are also observed. While specimens of both CD-T and FD-T fracture at M ~8.4 kN•mm, CD-NT fractures at a much higher M ~12 kN•mm. Similarly, CD-NT exhibits higher θ ~0.14 radians before fracture whereas CD-T and FD-T fracture at θ ~0.08 radians and ~0.10 radians, respectively.

In Fig. 5 (b), the variations in the magnitude of the abrupt θ excursions, $\Delta\theta_M$, as a function of the M at which they occur are plotted for the three BMGCs. Four θ excursions are observed in the M-θ plots of CD-NT, whereas three each are observed in those of CD-T and FD-T. While the first θ excursion occurs in the FD-T and CD-NT specimens when M ~1.4 kN•mm, CD-T specimen undergoes the first θ excursion when M is twice as high. Nevertheless, the magnitude of the θ excursion, $\Delta\theta_M$, is ~0.01 radians and same for all the BMGCs.

In the next θ excursion, $\Delta\theta_M$ increases to ~0.025 for CD-T and FD-T but is only ~0.02 for CD-NT. Moreover, this excursion occurs at a relatively low M of ~2.8 kN•mm for CD-NT but for the CD-T and FD-T BMGCs it occurs at M ~6.6 kN•mm and ~6 kN•mm, respectively. However, in the third θ excursion, while $\Delta\theta_M$ remains invariant for CD-NT, it reduces to ~0.01 radians for the other two BMGCs. The final θ excursion in CD-NT specimen is the largest with $\Delta\theta_M$ ~0.04 radians. As a result, the total $\Delta\theta_M$ in the M-θ plot of CD-T is ~0.09 radian, which is more than twice as high as that of CD-T and FD-T.

To understand the origin of intermittent surges in θ in the M-θ plots, we interrupted some of the fracture tests to observe the microstructures of the S4PB specimens. Fig. 6 (a)-(c) displays the optical images of the near notch regions of CD-NT, FD-T and CD-T specimens, respectively. Note that these images are obtained before the occurrence of the θ excursions at M ~8 kN•mm for CD-NT and M ~6 and ~6.3 kN•mm for FD-T and CD-T, respectively. In each specimen, multiple short, discontinuous, curved shear bands, which are distributed within three distinct lobes, originate from the notch tip. In CD-NT, one central lobe is oriented at ϕ ~0°, whereas two distal lobes are oriented at ϕ ~±56° from the notch line. While the central lobe is also present in FD-T and CD-T specimens, the distal lobes in them are oriented at ϕ ~±22° and ~±36°, respectively. The convention for measuring ϕ is shown in Fig. S4. On closer examination of these images, it is revealed that there are two families of shear bands, which are radial and tangential to the notch tip, within each lobe.

A broadly similar envelope of curved shear bands forms at the notch tips of mode I monolithic BMG specimens [33,35,37,39,40,59]. The main difference between these and those observed in BMGCs (Fig. 6 (a)-(c)) is that the former are longer and continuous. It is reported that the curvature of shear bands is an outcome of the elasto-plastic stress gradients prevalent near the notch tip. Tandaiya et al. numerically modelled the stress gradients and determined that they have continuous logarithmic spiral shapes [38,39]. They also suggested that since shear bands are the macroscopic carriers of plastic strain, their distribution will be function of the plastic strain variations along the notch profile. The envelope of these continuous shear bands constitutes the notch tip plastic zone in BMGs.

From the above, it is evident that in the presence of stress gradients near the notch tips, the BMG matrices in the BMGCs mediate the formation of curved shear bands. Moreover, it can be inferred that notch tip regions having a significant concentration of shear bands appear at locations with elevated levels of plastic strain. A magnified image of the near notch tip regions of the three BMGCs are shown in Fig. S5. While the continuity of shear bands is disrupted by the presence of dendrites in each BMGC, the average lengths of shear bands appear to be higher in CD-NT than that in CD-T and FD-T. The dendrites in the near notch tip regions of FD-T and CD-T specimens are further examined using TEM and their corresponding images are shown in the insets of Fig. S5 (b) and S5 (c), respectively. These images reveal that the β-Ti dendrites of these two BMGCs have undergone transformation to α”-Ti and As mentioned earlier (see Section 3.1) more dendrites in FD-T undergo α”-Ti transformation than that in CD-T specimens.

Fig. 6 (d)-(f) show the optical micrographs of the near notch regions of CD-NT, FD-T and CD-T specimens after the θ excursion. In each BMGC, it can be observed that several new shear bands grow ahead of the existing shear bands that emanated from the notch tips. In addition to this, in the CD-NT specimen, two additional distal lobes with concentrated shear bands form at the notch tips at ϕ ~81° and ~-22°. However, the same is not observed at the notch tips of the FD-T and CD-T specimens. It appears that the overall

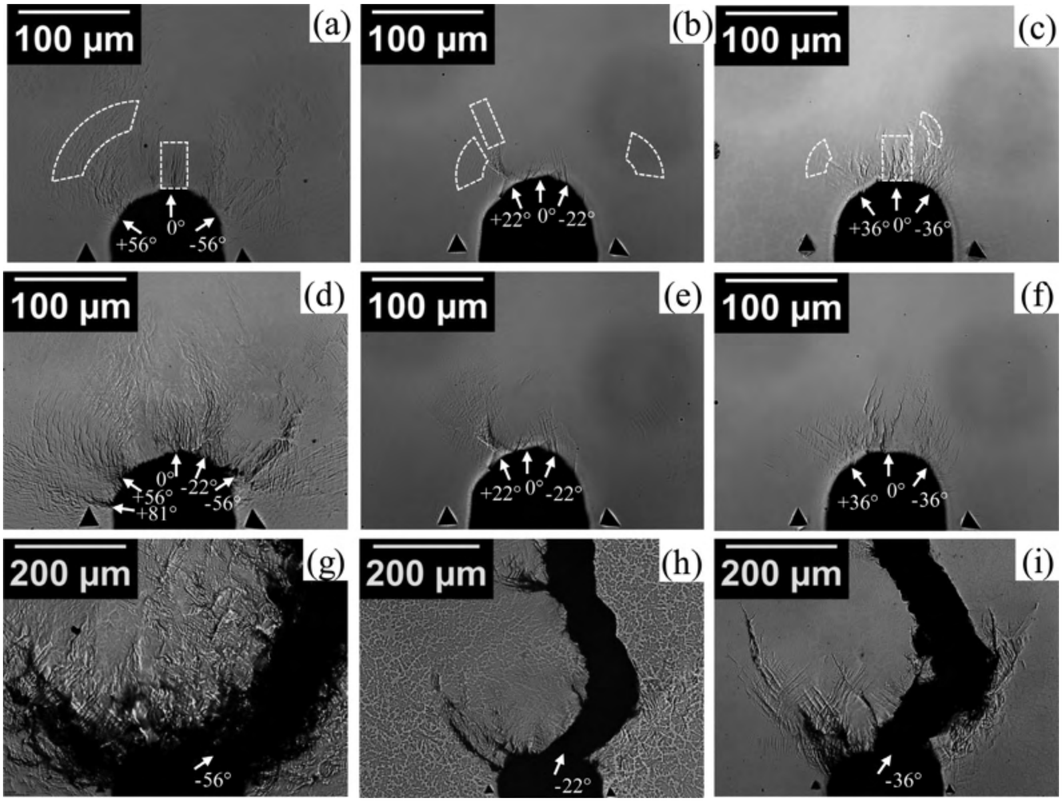

Fig. 6. Optical micrographs of the near notch tip regions in fracture specimens tested in mode I configuration (S4PB) of (a) CD-NT at M ~8 kN•mm, (b) FD-T at M ~6 kN • mm, and (c) CD-T at M ~6.3 kN • mm. Dashed boxes highlight two families of shear bands formed ahead of the notch tips. (d), (e), and (f) are images of the same regions in (a), (b), and (c), respectively, after θ excursions. (g), (h), and (i) are respective optical micrographs of the same regions after fracture.

shear band density at the notch tip of CD-NT is more profuse than that in FD-T and CD-T specimens.

Prior to fracture initiation, it is noted that the maximum extent of the plastic zone, r_p, in CD-NT is ~700 μm, whereas those of CD-T and FD-T are ~320 and ~260 μm, respectively (see Movie S1 (a), (b) and (c)). On comparing these with the thickness of the specimens (t ~3.5 mm), it is determined that plane strain conditions prevail in both CD-T and FD-T specimens but not in the CD-NT specimens [60,61].

In Fig. 6 (g)-(i), optical micrographs of the notch tip region of the fractured CD-NT, FD-T and CD-T specimens, respectively, are displayed. Note that in CD-NT specimen, although cracks nucleate along all the 5 shear band lobes on either side of the notch line, fracture finally occurs along ϕ ~-56°. Similarly, FD-T and CD-T specimens fracture via crack propagation along the shear band lobes oriented at ϕ ~-22° and ~-36°, respectively, although cracks nucleate within other shear band lobes as well. However, comparatively fewer cracks nucleate in the FD-T and CD-T specimens than that in the CD-NT specimens.

The θ excursions in Fig. 4 (a) are expected to have a significant influence on J_I as the latter is computed from the M-θ plots using Eq. (1). The variations of the computed J_I as a function of M are displayed in Fig. 7. With increasing M, the material accumulates increasing amounts of elastic strain energy that is eventually released during fracture. Since strain energy density is proportional to the square of strain, the variation of J_I with M is expected to be non-linear for all the BMGCs. However, due to the above-mentioned abrupt excursions in θ, the J_I-M plots also exhibit multiple discontinuities. Despite these discontinuities, variations in J_I and its rate of change with M is similar for the three BMGCs till $M < 6$ kN•mm. However, when M ~6 kN•mm, J_I abruptly increases to ~68 N/mm for FD-T but those of CD-T and CD-NT are only ~36 N/mm. When M increases from 6 N/mm to 8 N/mm, similar abrupt jumps in J_I are also observed for both CD-T and CD-NT, albeit at different M. This results in a crossover between the J_I-M curves of the three BMGCs at M ~8.3 kN•mm and J_I ~90 N/mm. Thereafter, FD-T and CD-T are unable to sustain further load and undergo fracture at J_I ~90.4 N/mm and 101.5 N/mm, respectively. In contrast, for CD-NT, J_I steadily increases to ~112 N/mm till M ~11.2 kN•mm and then abruptly increases to ~221.7 N/mm at M ~12 kN•mm, which is followed by fracture.

The critical energy release rate in mode I, J_{Ic}, for all BMGC specimens, except CD-NT, is estimated as the value of J_I that corresponds to the moment at fracture, M_c, in the J_I-M curves. Since plane strain conditions are not satisfied for CD-NT specimens, its J_I at M_c is designated as the conditional energy release rate, J_{IQ}. These values for the three BMGCs are listed in Table 3. While the FD-T and CD-T specimens have similar J_{Ic} of 90.4 N/mm and 101.5 N/mm, respectively, J_{IQ} of CD-NT is 221.7 N/mm. Since small scale yielding (SSY) conditions prevail at the notch tips of the two metastable β-Ti reinforced BMGCs, their linear elastic plane strain mode I fracture toughness, K_{Ic}, is calculated using, $K_{Ic}{}^2 = J_{Ic}.E/(1-\upsilon^2)$, where υ is the Poisson's ratio, and listed in Table 3. Although K_{Ic} cannot be estimated for CD-NT from the above-mentioned equations, mode I fracture data of DH3, which is compositionally and microstructurally equivalent to CD-NT, is already available in the literature [30]. As seen, CD-NT has the highest K_{Ic} ~157 MPa.m$^{0.5}$, whereas those of CD-T and FD-T are ~111.6 MPa.m$^{0.5}$ and ~105 MPa.m$^{0.5}$, respectively.

Overall, with increasing load, lobes of concentrated shear bands form at the notch tips of all the BMGCs. θ excursions in M-θ curves, that occur at constant M, only leads to elongation of these lobes in the FD-T and CD-T specimens, whereas in CD-NT specimen it also increases the number of shear band lobes at the notch tip.

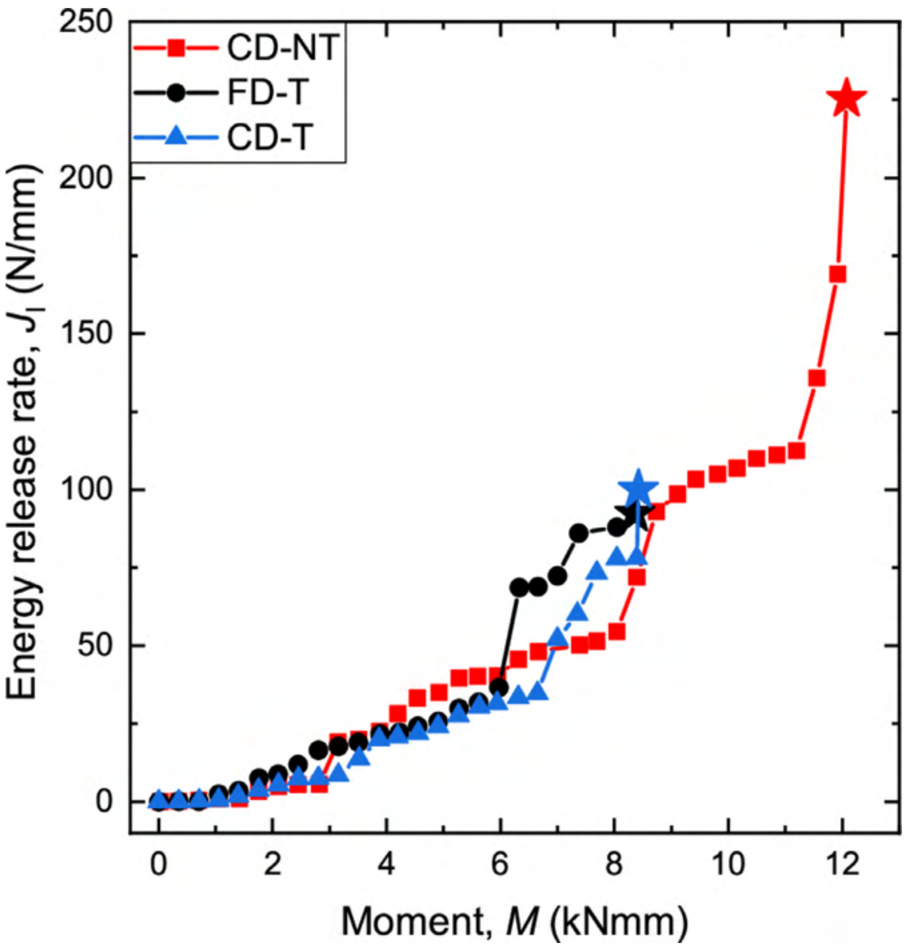

Fig. 7. Variations of J_I with M for mode I fracture specimens of the three BMGCs examined. Star symbols indicate the points of fracture initiation which coincide with catastrophic fracture.

Table 3
Energy release rate, fracture toughness, and width of fluid meniscus instability region of the BMGCs.

Material	J_{Ic} (or J_{IQ}) (N/mm)	K_{Ic} (MPa$\sqrt{m}$)	J_{IIc} (N/mm)	K_{IIc} (MPa$\sqrt{m}$)	J_{II}^{max}(N/mm)	ΔW (μm) Mode I	ΔW (μm) Mode II
CD-NT	221.7 (225.3, 218.1)	157 [30]	2.7 (2.5, 2.9)	17.6 (16.9, 18.2)	133.5 (136.9, 130.1)	95±37	100±28
FD-T	90.4 (92.3, 88.5)	105 (106.1, 103.9)	5.2 (4.9, 5.5)	25.2 (24.4, 25.9)	25.8 (27.4, 24.2)	89±26	–
CD-T	101.5 (100, 103)	111.6 (110.8, 112.4)	1.8 (1.6, 2.0)	14.9 (14, 15.7)	34.2 (33, 35.3)	108±43	89±23

Also, the BMGC where β-Ti transforms to α”-Ti during fracture, i.e., FD-T and CD-T, have lower mode I fracture toughness compared to that of the CD-NT, which has non-transforming β-Ti dendrites.

3.2.2. Energy release rate and notch tip plasticity in mode II fracture experiments

Fig. 8 (a) shows the representative V-δ_s responses obtained on notched AS4PB (mode II) specimens of the three BMGCs. In all the cases, V initially increases linearly with δ_s and then deviates from linearity. The V-δ_s plots of CD-T and FD-T specimen are smooth, unlike the M-θ curves of their S4PB specimens. Moreover, both specimen fracture at V ~ 5.2 kN, when δ_s ~70 μm. In contrast, the CD-NT specimen fractures at a higher V of ~7.7 kN. Moreover, its δ_s increases at a fixed V in two segments. The first and second segments occur at V ~4.6 and ~7.6 kN, where δ_s increases from ~47 to ~57 μm, and ~123 to ~190 μm, respectively.

The variations of the computed J_{II} as a function of V is shown for all the three BMGCs in Fig. 8 (b). Although the variations of J_{II} with V are also non-linear for all specimens, the J_{II}-V plots are smooth, unlike the J_I-M plots. In fact, until the fracture of CD-T and FD-T at V ~5.2 kN, the rate of increase of J_{II} with V is also same for the three BMGCs. Thereafter, J_{II} of CD-NT specimen increases steeply to 133.5 N/mm, which is nearly 4 times higher than the peak J_{II} of the other two BMGCs. Considerable stable crack growth is observed before catastrophic fracture.

To understand the processes leading to fracture, some AS4PB specimens of the BMGCs are unloaded at different V and examined under an optical microscope. Fig. 9 (a)-(c) displays the optical micrographs of the near notch regions of CD-NT, FD-T and CD-T specimens, respectively, after each of them is loaded to V ~7 kN. From real time videos of the fracture tests, it is observed that the notches of all BMGCs undergo sharpening on one part of the notch root and blunting on the other, which is expected in mode II loading conditions (See Movies S2 (a)-(c)). Multiple, straight and discontinuous shear bands, concentrated within distinct lobes, originate from the notch tips of all specimens. Moreover, in each specimen, one or two central lobes are oriented at ϕ ~±8°, whereas two distal lobes are oriented at ϕ ~±23° from the notch line. These shear band trajectories are also broadly similar to those that form at the notch tips of mode II monolithic BMG fracture specimens [33,34,39].

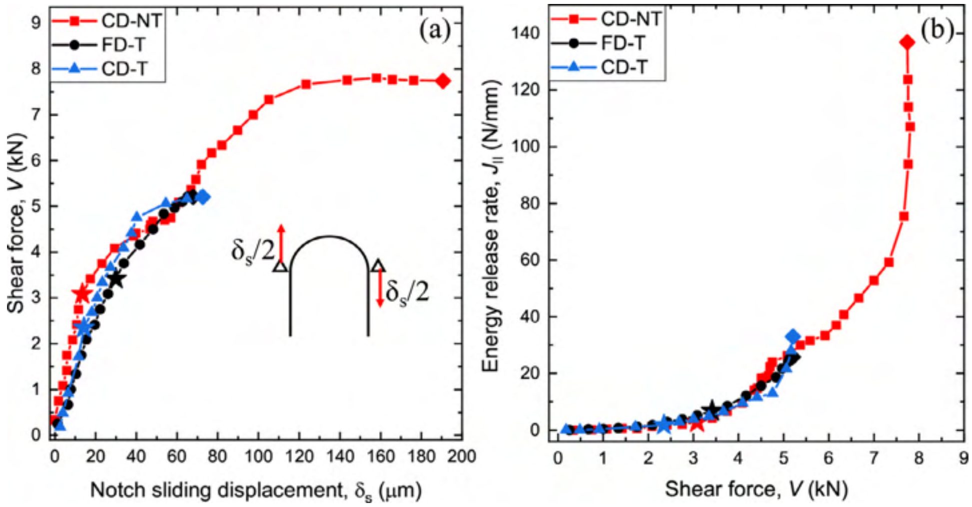

Fig. 8. (a) Variations of shear force, V, with notch sliding displacement, δ_s, and (b) J_{II} with V for mode II fracture specimens of CD-NT, FD-T, and CD-T. Star symbols indicate the points of fracture initiation.

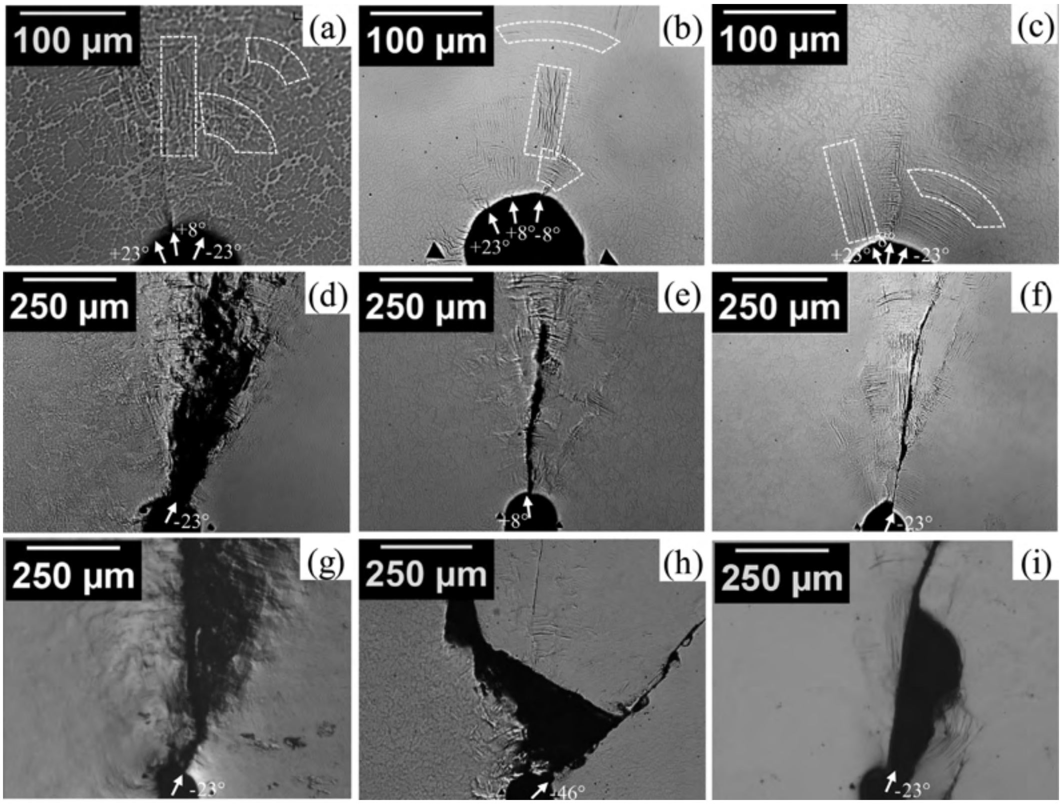

Fig. 9. Optical micrographs of the regions near the notch tip of (a) CD-NT, (b) FD-T, and (c) CD-T mode II fracture specimens (AS4PB) at V ~7 kN. (d), (e), and (f) are images of the same regions in (a), (b), and (c) respectively, at V ~14 kN. (g), (h), and (i) are optical images of regions near the notch tips of the same after fracture.

As V increases, the notch surfaces of all specimens further sharpen, and the existing shear bands grow in length. Eventually, the notch tip sharpens acutely and a crack initiates inside one of the shear bands. While the crack nucleates within the shear band lobe oriented at ϕ ~-23° from the notch line in both CD-NT and CD-T specimens, it nucleates within that oriented at ϕ ~+8° in the FD-T specimen. From the real time videos of the fracture tests, it is determined that the crack initiates at V ~3.1 and 2.3 kN in CD-NT and CD-T specimens, respectively, whereas in FD-T specimen, it occurs at a much higher V ~3.4 kN. At these values of V, it is determined that $r_p < 150$ μm at the notch tips of all BMGCs. Since this is much smaller than t, plane strain conditions can be assumed to prevail in all the mode II fracture tests [60,61]. Considering the V at which crack nucleates within the shear band as fracture initiation, the critical energy release rate for fracture in mode II, J_{IIc}, is estimated from the J_{II}-V curves of each BMGC and listed in Table 3. FD-T has the highest J_{IIc} of ~5.2 N/mm whereas that of CD-T and CD-NT are ~1.8 and ~2.7 N/mm, respectively. Applying the SSY approximation, the linear elastic mode II plane strain fracture toughness, K_{IIc}, for all BMGCs is also calculated using $K_{IIc}{}^2 = J_{IIc}.E/(1-\upsilon^2)$. The trend in the variation of K_{IIc} is same as that observed for J_{IIc}.

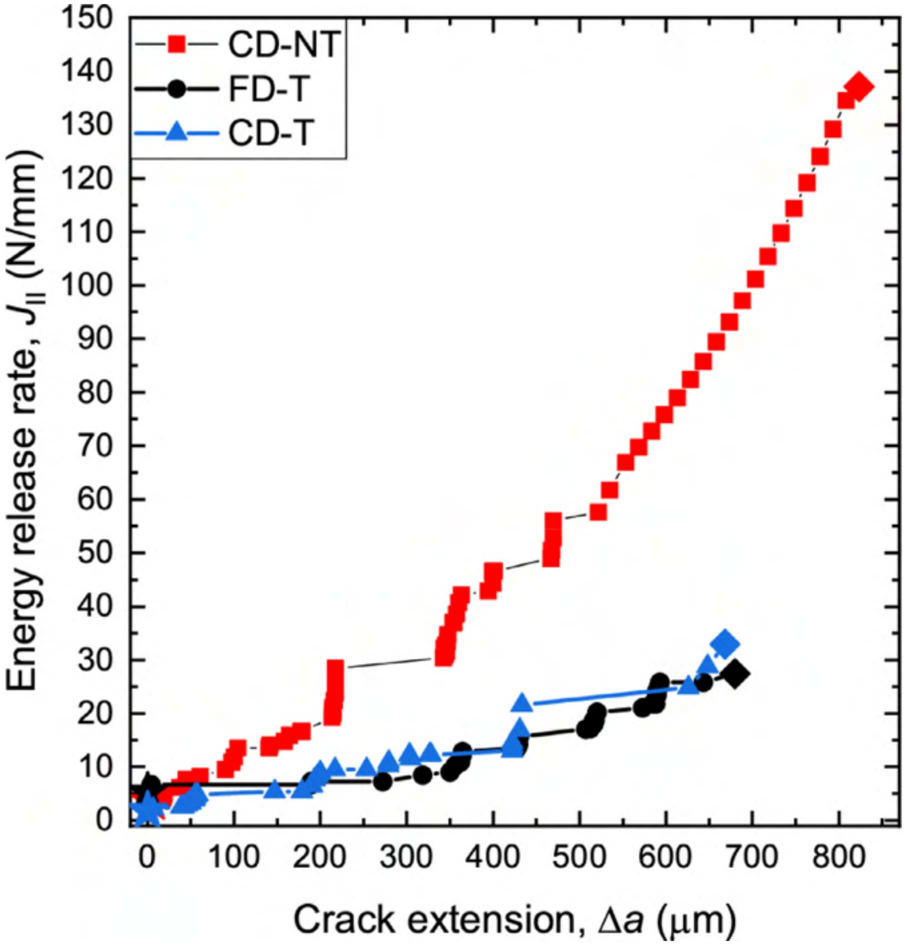

Fig. 10. Variations of J_{II} with crack extension, Δa, of CD-NT, FD-T, and CD-T mode II fracture specimens.

Upon further loading, the cracks, which nucleated within the shear band lobes of the BMGCs, grow stably. Optical micrographs of the near notch regions of CD-NT, FD-T and CD-T specimens at V ~14 kN, shown in Fig. 9 (d)-(f), reveal that cracks grow to significant lengths before fracture occurs. Fig. 9 (g)-(i) show the optical micrographs of the notch tip regions of the fractured CD-NT, FD-T and CD-T AS4PB specimens, respectively, after putting them back together. While fracture of CD-NT and CD-T specimens occurs along the growing crack observed in Fig. 9 (d) and (f), FD-T fractures via the propagation of a new crack that is oriented at ϕ ~-46° from the notch line. However, the regions surrounding the crack in CD-NT are significantly deformed, compared to those in the other two BMGCs. Also, post-facto TEM imaging of the notch tip regions of the fractured mode II FD-T and CD-T specimens reveal that β-Ti dendrites in them transform to α"-Ti, much like that seen in their mode I counterparts.

The variations in J_{II} are plotted as a function of the change in crack length, Δa, for each BMGC in Fig. 10. All the three BMGCs exhibit increasing fracture resistance with crack extension, which is also referred to as R-curve behaviour. In all the R-curves, there are several segments where J_{II} increases sharply at constant Δa, which is immediately followed by a sharp excursion in Δa at constant J_{II}. Nevertheless, the overall rate of change of J_{II} with Δa and the number of J_{II} excursions is highest for CD-NT, while those of the other two composites are much lower. Alternately, the average magnitudes of Δa excursions, Δa_{avg}, follows the reverse trend. The Δa_{avg} of CD-NT specimens is 53.4 ± 31.6 μm, whereas those of FD-T and CD-T are 91.3 ± 43.4 μm and 88.1 ± 58.7 μm, respectively. Following intermittent occurrences of crack arrest, the maximum crack extension, Δa_{max}, for CD-NT is ~823 μm, whereas it is slightly lesser than 700 μm for the other two BMGCs. Moreover, the CD-NT specimen exhibits the highest peak fracture resistance, J_{II}^{max} ~133.5 N/mm, which is more than 4 times higher than J_{II}^{max} of the two metastable BMGCs.

Fig. S6 (a)-(c) shows the notch tip SEM images of the mode II specimens of CD-NT, FD-T and CD-T, respectively, before the occurrence of a J_{II} excursion in their respective R-curves. In all the three alloys, a crack arrested at a dendrite is observed, which implies that J_{II} excursions corresponds to crack arrest. Also, several shear bands are observed in regions ahead of the arrested crack tip.

Overall, although J_{IIc} corresponding to fracture initiation is highest for the FD-T, CD-NT exhibits the highest fracture resistance with crack extension. Broadly, the formation of shear band lobes ahead of the notch tip and the nucleation of cracks within one of them are some of the many similarities between mode I and mode II fracture behaviour of the BMGCs. However, the following distinctions between the two must also be noted. For all BMGCs, the mode II fracture toughness and J_{II}^{max} are lower than mode I fracture toughness. Moreover, stable crack growth and fracture resistance behaviour with crack extension is observed only in mode II loading conditions.

3.2.3. Fractographic observations

Representative low magnification SEM images of the fracture surfaces of CD-NT, FD-T and CD-T notched S4PB (mode I) specimens are shown in Fig. 11 (a)-(c). Two distinct fracture morphologies are identified in each of them and their boundaries are

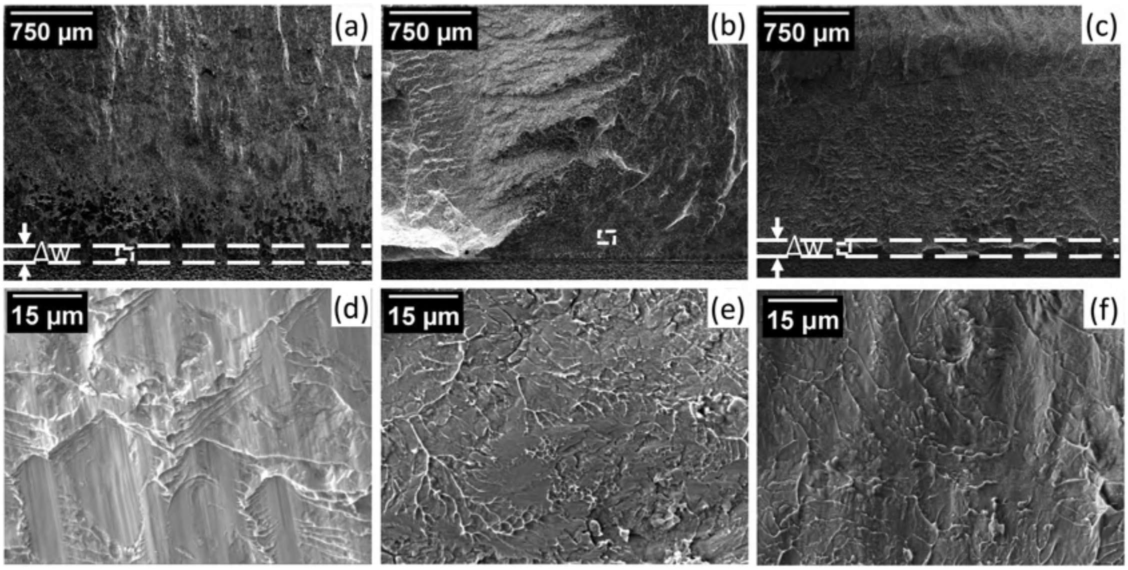

Fig. 11. Low magnification SEM images of the regions near the notch front in the mode I fracture specimens of (a) CD-NT, (b) FD-T, and (c) CD-T BMGCs. (d), (e), and (f) are magnified SEM images of the regions enclosed within the dashed boxes in (a), (b), and (c), respectively.

marked in the images. The one close to the notch tip region is labelled as region A whereas the other is region B. Fig. 11 (d)-(e) display the magnified images of region A from the fracture surfaces of CD-NT, FD-T and CD-T, respectively. Region A is flat and contains ridges that extend along the crack growth direction. In contrast, region B consists of coarse dimples and rough features, which typically form due to unstable crack propagation.

Tandaiya et al. [33,39] observed similar fractographic features in their mode I notch fracture experiments on Zr-based BMGs. However, in BMGs, in addition to the above-mentioned regions, a notch blunting region, located adjacent to the notch tip, is also observed. They analysed the features in each region and provided the following explanation for their existence. On loading a notched BMG S4PB specimen, the notch tip blunts when shear bands start nucleating from it. Further loading facilitates the formation of an incipient crack inside a dominant shear band. Since structural disorder and adiabatic temperature rise within shear bands makes the material inside them ‘liquid-like’, the fracture surface features could be explained by considering the separation mechanism of liquids bounded by solid surfaces [39]. The notch surface behaves like a fluid meniscus and grows within the dominant shear band in the presence of a positive hydrostatic stress gradient. During this, the meniscus breaks into channels, which appear as cylindrically shaped ridges on the fracture surface, much like those observed in region A of all BMGC specimen fracture surfaces (see Fig. 11 (d)-(e)). Although the hydrostatic stress within the dominant shear band increases along its length, at some critical length, l_c, the pressure gradient becomes negative. Therefore, when the amplitude of fluid meniscus perturbations equals l_c, the meniscus becomes unstable and leads to unstable crack propagation and fast fracture. From this mechanistic point of view, it is evident that region A in the BMGCs correspond to processes involving fluid meniscus instability (FMI) and will hence be referred to as the FMI region. Similarly, region B will be referred to as the fast fracture region. Moreover, l_c corresponds to the characteristic width, ΔW, of the FMI region for each BMGC.

Since the above discussion suggests that the width of FMI plays an important role in fracture initiation, the average ΔW of all the three BMGCs is measured from their fractographic images and listed in Table 3. For CD-NT, FD-T and CD-T, ΔW are 95 ± 37, 89 ± 26, and 108 ± 43 μm, respectively. Note that no correlation between ΔW and J_{Ic} could be ascertained as the former is nearly the same for all the BMGCs.

Low magnification SEM images of the fracture surfaces of CD-NT, FD-T and CD-T notched AS4PB (mode II) specimens are displayed in Fig. 12 (a)-(c). While both the above-mentioned fracture morphologies are present in CD-NT and CD-T specimens, they were not seen on the fracture surface of the FD-T specimen. Moreover, the ridge like morphology observed in the FMI region of mode I specimens is not present in the mode II specimens of CD-NT. Instead, the region close to the notch tip contains relatively flat features and ploughing marks. According to Tandaiya et al. [39], the fracture mechanism in mode I and mode II loading conditions are similar, i.e., the growth of a fluid meniscus inside a dominant shear band is followed by unstable crack growth due to the change in the nature of the pressure gradient. The only difference is that the crack faces of mode II specimens slide over each other, which may lead to the smearing of features and the formation of ploughing marks. From this, it is evident that the FMI regions formed near the notch tip of CD-NT and CD-T mode II specimens are also lost to the rubbing of crack faces. However, despite the loss of these characteristic features, the FMI region of mode II specimens could be broadly measured by carefully observing the transition in fracture features. Values of ΔW for CD-NT and CD-T, which are also listed in Table 3, are 100 ± 28 and 89 ± 23 μm, respectively.

The fracture of FD-T specimen is unique as the fracture surface contains FMI-like ridge like patterns at several locations on the fracture surface. This is possibly a consequence of the fact that although a crack initiates and grows along the shear bands oriented at ϕ ~+8° from the notch line in the FD-T specimen, final fracture occurs along ϕ ~-46°. Note that a crack oriented at ϕ ~-46° from the notch line in mode II, experiences mode I loading conditions. Since this prevents rubbing of the surfaces, the ridge like features on the fracture surface are preserved. However, fracture along this trajectory also results in the loss of the characteristic features associated with the growth of the stable crack oriented at ϕ ~+8°.

Nevertheless, the trends so far suggest that ΔW for all the three BMGCs are in the range of 85-105 μm, in both mode I and mode II loading conditions. Interestingly, these match well with the ΔW of monolithic BMGs, such as Vit 1, Vit 105 and $Zr_{70}Ni_{16}Cu_6Al_8$ BMGs, which are 60, 80, and 110 μm, respectively [37,39,41]. Finally, the absence of brittle fracture features such as flat surfaces or “mirror-

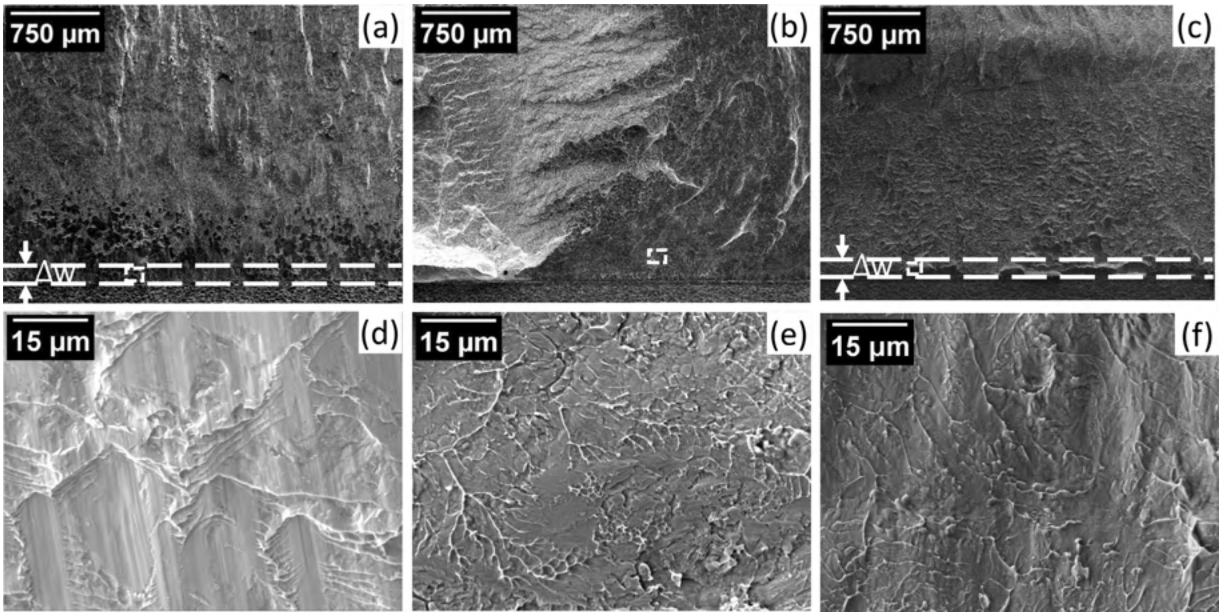

Fig. 12. Low magnification SEM fractographs of the regions near the notch front in the mode II fracture specimens of (a) CD-NT (b) FD-T, and (c) CD-T BMGCs. (d) (e), and (f) are magnified SEM images of the regions enclosed within the dashed boxes in (a), (b), and (c) respectively.

mist"-like morphologies in all BMGC specimens indicates that the mode I and mode II fracture in them is ductile.

4. Discussion

Owing to the similarities between the notch tip profiles, the magnitudes of ΔW, and fractographic images of BMGs and BMGCs specimens, irrespective of the loading mode, it is reasonable to expect that their fracture criterion and mechanisms would also be broadly similar. Applying the strain-based criterion for ductile fracture of BMGs to BMGCs, it can be said that fracture initiates when the plastic strain within a dominant shear band exceeds a critical value, ε_c, over the critical radial distance l_c (~ ΔW) from the notch tip. Experimental observations suggest that ΔW for all BMGCs is similar, irrespective of the loading mode. Moreover, given that the major chemical constituents in all the BMGCs are Zr and Ti, it is reasonable to assume that they would have a similar ε_c [36,37,39].

However, the variations in fracture toughness of the BMGCs can be rationalized by examining the influence of β-Ti dendrites on the fracture processes. First, upon loading the fracture specimens, plastic deformation initiates in the dendrites close to the notch tip as they are softer than the matrix. As mentioned earlier, the breakdown of strain compatibility between the dendrite and matrix leads to the nucleation of shear bands. Although the elasto-plastic stress field ahead of the notch tip guides the propagation of shear bands, they are arrested by the β-Ti dendrites, which shorten their lengths. This, in turn, reduces both the magnitude of their shear offsets and the amount of plastic deformation that can be accommodated by them. To compensate for the latter, several additional short shear bands form. The dense network of short shear bands forming within wide lobes, in front of the notch tips of mode I and mode II BMGC specimens, is attributed to this phenomenon (see Figs. 6 and 9).

The formation of the above-described wide lobes of short shear band at the notch tips has different implications for fracture initiation in mode I and mode II specimens of BMGCs. In mode I specimens, as M increases, these wide lobes of distributed shear bands accommodate plastic deformation homogeneously and ensures uniform blunting of the notch tip. The basis for this assertion is the observation that each excursion in θ, which is an outcome of notch tip blunting, in the M-θ curves of the BMGCs is accompanied by an increase in the spread of the shear band clusters at the notch tips (compare Fig. 6 (a)-(c) and 6 (d)-(f)). Since the notch tip plastic strain is distributed amongst numerous other shear bands, the shear band to crack transition is deferred, which culminates as an enhancement in J_I. It is also worth mentioning here that there is a critical difference in the characteristics of notch blunting in BMGs and BMGCs. While notch tips in BMGs undergo discrete blunting by shear bands, those in the BMGCs blunt more uniformly, which also explains the absence of a distinct notch blunting zone in them (see Fig. 11).

From this discussion, a direct link between the extent of notch blunting, via the spreading and widening of shear band lobes, and a higher J_{Ic} can be established. As the notch tip of CD-NT specimens undergoes several stages of notch blunting, it expectedly has the highest J_{Ic} of the three composites. It is however worth enquiring why the mode I specimens of CD-T and FD-T undergo modest levels of notch blunting despite containing transforming β-Ti dendrites, which as mentioned earlier, strain harden significantly and are more effective in arresting shear bands and reducing their lengths (see Fig. 4 (b)-(d) and Fig. S5 (a)-(c)). Their shorter lengths should, in principle, also imply that they bear lower plastic strains.

It is possible to rationalize the above observations by considering the differences in the structural states of the matrices of the BMGCs. As mentioned earlier, the ΔH_{rel} is a measure of the structural states of the BMGCs (see Section 3.1). A higher ΔH_{rel} corresponds to greater structural disorder, which also translates to higher excess free volume in the amorphous phase. A higher excess free volume content reduces the barrier for activation of shear transformation zones (STZs), which are the unit carriers of plasticity in BMGs. Since the activation and linking up of STZs leads to the formation of macroscopic shear bands, a higher excess free volume promotes profuse shear banding [4]. Therefore, the BMGC whose matrix has higher ΔH_{rel} is likely to nucleate a greater number of shear bands. Since ΔH_{rel} of CD-NT BMGC is more than twice and thrice as high as that of CD-T and FD-T BMGCs, respectively, for the same plastic strain, the former is more likely to nucleate more shear bands. This is indeed found to be true as the number of shear band lobes and their relative spread is highest at the notch tip of the CD-NT mode I specimen (see Fig. 6 (a)).

An important consequence of the lower shear band density ahead of the notch tips of CD-T and FD-T specimens is that strain partitioning amongst these shear bands results in greater plastic strain accommodation by each of them. This also implies that these shear bands will have larger shear offsets than those in CD-NT specimens. The relatively darker contrast of shear bands in the two tensile-tested metastable β-Ti reinforced BMGCs, displayed in Fig. 4 (b) and (c), lends support to this conjecture. Owing to larger shear offsets, it is reasonable to expect that the transition from shear bands to shear cracks in the two metastable β-Ti reinforced BMGCs, would occur at lower M. However, this does not imply that the transforming dendrites in the two metastable β-Ti reinforced BMGCs do not have any influence on the fracture mechanism. In fact, the initial higher rate of increase of J_I at M ~6 kN•mm in the FD-T and CD-T mode I specimens, compared to that of the CD-NT specimen, is attributed to the transformation of their dendrites and their effectiveness in mitigating shear band propagation. However, as discussed above, their matrices of these two alloys, which have lower ΔH_rel, are incapable of nucleating more shear bands to accommodate the increasing plastic strain. Consequently, the plastic strain is accommodated by the growth of shear offsets in the previously arrested shear bands, which then rapidly transform to cracks. This also implies that FD-T and CD-T BMGCs would have been much tougher than CD-NT if their matrices had higher ΔH_rel.

In mode II specimens, although lobes of short shear bands also form in front of the notch tips, they blunt only one portion of the notch surface while the other sharpens. Note that this is distinctly different than the symmetric and uniform blunting of that notch tip observed in mode I BMGC specimens. Owing to the partial blunting of the notch tip by the shear band lobes, the sharp portion of the notch surface grows into one of the shear bands and transforms rapidly into a crack. As crack nucleation within shear bands occurs at relatively lower loads in the mode II specimens, the ability of dendrites to limit the growth of shear bands will have a greater influence on J_IIc. Of the three BMGCs, the dendrites in FD-T are most effective in limiting shear bands to the smallest lengths as, apart from undergoing deformation induced transformation that block the propagation of shear bands, they also have the lowest interdendritic spacing (λ). Since the plastic strain within these shear bands will not be sufficient to enable crack nucleation, J_IIc of FD-T is expectedly the highest.

It is also observed that, for all BMGCs, J_IIc is substantially lower than J_Ic. Several studies noted the same trend in BMGs [32,33] and attributed it to the relative ease of crack nucleation inside a shear band when the loading is shear dominant. Since fracture initiation in BMGCs also occurs via the same crack nucleation mechanism, the above-mentioned argument can be applied to justify the differences in their mode II and Mode I fracture toughness.

In fact, this difference in the ease of crack nucleation within shear bands is partly responsible for the crack growth resistance behaviour observed in mode II specimens but not in mode I specimens. In mode I specimens, the uniform and symmetric blunting of the notch tip, on loading, delays fracture initiation as a discrete shear offset for mediating crack nucleation at the notch tip is unavailable. Therefore, crack nucleation only occurs when the strain within one or more of the shear bands ahead of the notch tip intersect the notch surface creating a large offset. Since this occurs when the plastic strain within the shear bands is close to ε_c, crack nucleation in mode I specimens is immediately followed by catastrophic crack propagation.

In contrast, the partial sharpening of the notch tip in mode II specimens allows rapid nucleation of an incipient crack within one of the shear bands at much lower loads. However, owing to the strain partitioning between the numerous short shear bands, plastic strains within individual bands are significantly lower than ε_c. As plastic strain increases along this shear band, the incipient crack within it also undergoes partial blunting and sharpening. This results in the formation of new shear bands ahead of the incipient crack tip (see Fig. S6 (a)-(c)). As the incipient crack terminates on dendrites, its growth can proceed only after cutting through the latter. In the meantime, the newly formed shear bands also evolve into incipient cracks with increasing strain. The process of crack nucleation within shear bands, followed by their partial sharpening and blunting, repeats itself several times and leads to the segmented growth of cracks in the mode II specimens of BMGCs (see Fig. S6 (d)-(e)). The bridging of cracks by the ligaments and dislocation mediated plastic deformation of the dendrites within the ligaments facilitates greater fracture resistance. This manifests as steep increases in J_II at fixed Δa, which is observed in the R-curves displayed in Fig. 10. In contrast, discrete excursions in Δa at a fixed J_II are observed, when the crack segments connect with each other after cutting through the dendrites. A close match between the average lengths of the Δa excursions and λ, δ of all BMGCs supports this conjecture.

Nevertheless, while the above-mentioned mechanism is applicable to all the studied BMGCs, it is worth examining the underlying cause for the variations in the slopes of J_II-Δa curves. We believe that this particular aspect is also governed by the structural state of the matrix. As mentioned earlier, the relatively low ΔH_rel of the matrices of FD-T and CD-T restricts the formation of shear bands ahead of the notch tip. Due to limited plastic strain partitioning, cracks mature quickly within them and connect with each other at lower loads. This leads to much larger Δa excursions in them than that observed in CD-NT specimen and eventually manifests as differences in the steepness of their R-curves.

Before closing, it is worth reiterating that the structural state of the BMGC matrices has a more dominant influence on the mode I and mode II fracture toughness and crack growth resistance of the BMGCs than their dendrites. It is also noted that, CD-T and FD-T would probably be tougher than CD-NT if their matrices had higher ΔH_rel. This is indeed surprising as the dendrite characteristics dictate strain hardening rate and ε_u of these BMGCs in uniaxial tension. Nevertheless, in the context of improving fracture toughness of BMGCs, it is important to understand the ways to increase ΔH_rel of the matrices. A higher rate of cooling of the alloy from its melt ensures greater structural disorder in the room temperature glassy phase, which translates to greater ΔH_rel of the matrix. However, there are two possible limitations on varying the cooling rate of the alloys by a large extent. First, it is likely that a higher cooling rate during solidification may result in supersaturation of some constituents in the matrix and lead to undesirable changes in the precipitation kinetics of dendrites. Second, owing to the temperature gradient that is present from the surface to the core of the casting, restrictions on the critical casting size are inevitable. A good alternative for manipulating the ΔH_rel of the matrix is to employ the post-solidification heat treatments such as cryo-cycling and flash annealing, which involves short-term annealing in the supercooled liquid regime. These techniques have hitherto been applied to BMGs and a good degree of enhancement of shear band plasticity has also been observed. However, whether these methods will indeed improve the fracture toughness of BMGCs is unknown and a topic for future studies.

5. Summary and conclusions

The microstructure and tensile properties of three β-Ti reinforced Zr/Ti-based BMGCs, distinguished by the length scales, composition and transforming nature of their dendrites, are evaluated. Mode I and mode II fracture experiments on these BMGCs are performed with the objective of understanding the influence of microstructural length scales and deformation-induced transformation of dendrites on fracture mechanisms. Systematic imaging of the notch tip profile indicates that although β-Ti dendrites alleviate strains associated with the shear bands, the fracture mechanisms in BMGCs and BMGs are broadly similar, i.e., the fluid meniscus instability criterion governs transition of a shear band to a shear crack, in both modes of loading. Stable crack growth and increasing fracture resistance behaviour is observed in mode II specimens when the cracks are arrested by dendrites. However, the same is not observed in mode I specimens as they have higher crack initiation resistance compared to mode II specimens. BMGCs which contain β-Ti dendrites that undergo martensitic transformation are more effective in arresting propagating shear bands. Although this is expected to improve the fracture toughness of these BMGCs by delaying the shear band to crack transition, the BMGC containing non-transforming β-Ti dendrites have higher mode I and mode II fracture toughness. This surprising result is the outcome of lower relaxation enthalpy of the BMG matrix in BMGCs that contain transforming β-Ti dendrites. The lower relaxation enthalpy of the matrix reduces the degree of shear banding in the matrix, which in turn facilitates shear band to crack transition at smaller strains. Therefore, if the structural state of the matrix is manipulated to increase its propensity to form shear bands, the mode I and mode II fracture toughness of BMGCs reinforced with transforming β-Ti dendrites will significantly improve.

Declaration of Competing Interest

The authors declare that they have no known competing financial interests or personal relationships that could have appeared to influence the work reported in this paper.

Acknowledgements

RLN's research at IITD was supported through the Start-up research grant (SRG/2020/000095) of Science and engineering research board, DST, GoI. DR's visit to NTU, where all the experiments reported in this work were conducted, was supported by an IITB-NTU joint PhD Degree Program. The work at Nanyang Technological University was supported by the funding from A*STAR via the Structural Metals and Alloys Programme (No. A18B1b0061). The work at Institute of Metal Research CAS was supported by the National Natural Science Foundation of China (51701213 and 51790484), the Chinese Academy of Sciences (ZDBS-LY-JSC023) and the Youth Innovation Promotion Association CAS.

Supplementary materials

Supplementary material associated with this article can be found, in the online version, at doi:10.1016/j.actamat.2021.116963.

References

[1] C.A. Schuh, T.C. Hufnagel, U. Ramamurty, Mechanical behavior of amorphous alloys, Acta Mater. 55 (2007) 4067–4109, doi:10.1016/j.actamat.2007.01.052.
[2] J. Xu, U. Ramamurty, E. Ma, The fracture toughness of bulk metallic glasses, JOM 62 (2010) 10–18, doi:10.1007/s11837-010-0052-4.
[3] U. Ramamurty, S. Jana, Y. Kawamura, K. Chattopadhyay, Hardness and plastic deformation in a bulk metallic glass, Acta Mater. 53 (2005) 705–717, doi:10.1016/j.actamat.2004.10.023.
[4] P. Murali, U. Ramamurty, Embrittlement of a bulk metallic glass due to sub-Tg annealing, Acta Mater. 53 (2005) 1467–1478, doi:10.1016/j.actamat.2004.11.040.
[5] A.L. Greer, Y.Q. Cheng, E. Ma, Shear bands in metallic glasses, Mater. Sci. Eng. R Rep. 74 (2013) 71–132, doi:10.1016/j.mser.2013.04.001.
[6] T. Mukai, T.G. Nieh, Y. Kawamura, A. Inoue, K. Higashi, Dynamic response of a Pd40Ni40P20 bulk metallic glass in tension, Scr. Mater. 46 (2002) 43–47, doi:10.1016/S1359-6462(01)01193-9.
[7] Z.. Zhang, J. Eckert, L. Schultz, Difference in compressive and tensile fracture mechanisms of Zr59Cu20Al10Ni8Ti3 bulk metallic glass, Acta Mater. 51 (2003) 1167–1179, doi:10.1016/S1359-6454(02)00521-9.
[8] R.L. Narayan, L. Tian, D. Zhang, M. Dao, Z.W. Shan, K.J. Hsia, Effects of notches on the deformation behavior of submicron sized metallic glasses: insights from in situ experiments, Acta Mater. 154 (2018) 172–181, doi:10.1016/j.actamat.2018.05.041.
[9] D.C. Hofmann, Bulk metallic glasses and their composites: a brief history of diverging fields, J. Mater. (2013) 2013, doi:10.1155/2013/517904.
[10] P.S. Singh, R.L. Narayan, I. Sen, D.C. Hofmann, U. Ramamurty, Effect of strain rate and temperature on the plastic deformation behaviour of a bulk metallic glass composite, Mater. Sci. Eng. A (2012), doi:10.1016/j.msea.2011.11.096.
[11] S. Gouripriya, P. Tandaiya, Three-dimensional unit cell study of a porous bulk metallic glass under various stress states, J. Appl. Mech. 86 (2019) 61010, doi:10.1115/1.4042995.
[12] T. Wada, A. Inoue, A.L. Greer, Mechanical properties of porous bulk glassy alloy prepared in high-pressure hydrogen atmosphere, Mater. Sci. Eng. A 448–451 (2007) 958–961, doi:10.1016/j.msea.2006.02.337.
[13] J.W.W. Qiao, a.C.C. Sun, E.W.W. Huang, Y. Zhang, P.K.K. Liaw, C.P.P. Chuang, Tensile deformation micromechanisms for bulk metallic glass matrix composites: from work-hardening to softening, Acta Mater. 59 (2011) 4126–4137, doi:10.1016/j.actamat.2011.03.036.
[14] M.Q. Tang, H.F. Zhang, Z.W. Zhu, H.M. Fu, A.M. Wang, H. Li, Z.Q. Hu, TiZr-base bulk metallic glass with over 50 mm in diameter, J. Mater. Sci. Technol. 26 (2010) 481–486, doi:10.1016/S1005-0302(10)60077-1.
[15] R.L. Narayan, P.S. Singh, D.C. Hofmann, N. Hutchinson, K.M. Flores, U. Ramamurty, On the microstructure–tensile property correlations in bulk metallic glass matrix composites with crystalline dendrites, Acta Mater. 60 (2012) 5089–5100, doi:10.1016/j.actamat.2012.06.032.
[16] L. Zhang, R.L. Narayan, H.M. Fu, U. Ramamurty, W.R. Li, Y.D. Li, H.F. Zhang, Tuning the microstructure and metastability of β-Ti for simultaneous enhancement of strength and ductility of Ti-based bulk metallic glass composites, Acta Mater. 168 (2019) 24–36, doi:10.1016/j.actamat.2019.02.002.
[17] L. Zhang, Z. Zhu, H. Fu, H. Li, H. Zhang, Improving plasticity and work-hardening capability of β-type bulk metallic glass composites by destabilizing β phases, Mater. Sci. Eng. A 689 (2017) 404–410, doi:10.1016/J.MSEA.2017.02.070.
[18] L. Zhang, R.L. Narayan, B.A. Sun, T.Y. Yan, U. Ramamurty, J. Eckert, H.F. Zhang, Cooperative shear in bulk metallic glass composites containing metastable β-Ti dendrites, Phys. Rev. Lett. (2020), doi:10.1103/PhysRevLett.125.055501.
[19] D.C. Hofmann, J.-Y. Suh, A. Wiest, G. Duan, M. Lind, M.D. Demetriou, W.L. Johnson, Designing metallic glass matrix composites with high toughness and tensile ductility, Nature 451 (2008) 1085–1089, doi:10.1038/nature06598.
[20] H. Choi-Yim, R. Busch, W.L. Johnson, The effect of silicon on the glass forming ability of the Cu47Ti34Zr11Ni8 bulk metallic glass forming alloy during processing of composites, J. Appl. Phys. 83 (1998) 7993–7997.
[21] H. Choi-yim, R.D. Conner, F. Szuecs, W.L. Johnson, Processing, microstructure, and properties of ductile metal particulate reinforced Zr57Nb5Al10Cu15.4Ni12.6 bulk metallic glass composites, Acta Mater. 50 (2002) 2737–2745, doi:10.1016/S1359-6454(02)00113-1.
[22] C.C. Hays, C.P. Kim, W.L. Johnson, Microstructure controlled shear band pattern formation and enhanced plasticity of bulk metallic glasses containing in situ formed ductile phase dendrite dispersions, Phys. Rev. Lett. 84 (2000) 2901–2904, doi:10.1103/PhysRevLett.84.2901.
[23] X.Z. Ma, D.Q. Ma, H. Xu, H.Y. Zhang, M.Z. Ma, X.Y. Zhang, R.P. Liu, Enhancing the compressive and tensile properties of Ti-based glassy matrix composites with Nb addition, J. Non. Cryst. Solids 463 (2017) 56–63, doi:10.1016/j.jnoncrysol.2017.02.025.
[24] S. Gouripriya, P. Tandaiya, Mechanistic origins of work hardening in shape memory alloy particle reinforced ex-situ bulk metallic glass matrix composites, Scr. Mater. 185 (2020) 1–6, doi:10.1016/j.scriptamat.2020.04.013.
[25] R.L. Narayan, K. Boopathy, I. Sen, D.C. Hofmann, U. Ramamurty, On the hardness and elastic modulus of bulk metallic glass matrix composites, Scr. Mater. 63 (2010) 768–771, doi:10.1016/j.scriptamat.2010.06.010.
[26] M.N..N.M. Patnaik, R. Narasimhan, U. Ramamurty, Spherical indentation response of metallic glasses, Acta Mater. 52 (2004) 3335–3345, doi:10.1016/j.actamat.2004.03.028.
[27] S. Jana, U. Ramamurty, K. Chattopadhyay, Y. Kawamura, Subsurface deformation during Vickers indentation of bulk metallic glasses, Mater. Sci. Eng. A 375–377 (2004) 1191–1195, doi:10.1016/j.msea.2003.10.068.
[28] D.C. Hofmann, J.-Y. Suh, A. Wiest, M.-L. Lind, M.D. Demetriou, W.L. Johnson, Development of tough, low-density titanium-based bulk metallic glass matrix composites with tensile ductility, Proc. Natl. Acad. Sci. USA 105 (2008) 20136–20140, doi:10.1073/pnas.0809000106.
[29] R. Raghavan, V.V Shastry, A. Kumar, T. Jayakumar, U. Ramamurty, Toughness of as-cast and partially crystallized composites of a bulk metallic glass, Intermetallics 17 (2009) 835–839, doi:10.1016/j.intermet.2009.03.012.
[30] M.E. Launey, D.C. Hofmann, J.-Y.Y. Suh, H. Kozachkov, W.L. Johnson, R.O. Ritchie, Fracture toughness and crack-resistance curve behavior in metallic glass-matrix composites, Appl. Phys. Lett. 94 (2009) 241910, doi:10.1063/1.3156026.
[31] M.E. Launey, D.C. Hofmann, W.L. Johnson, R.O. Ritchie, Solution to the problem of the poor cyclic fatigue resistance of bulk metallic glasses, in: Proc. Natl. Acad. Sci., 2009, doi:10.1073/pnas.0900740106.
[32] R. Narasimhan, P. Tandaiya, I. Singh, R.L. Narayan, U. Ramamurty, Fracture in metallic glasses: mechanics and mechanisms, Int. J. Fract. (2015), doi:10.1007/s10704-015-9995-3.
[33] P. Tandaiya, U. Ramamurty, R. Narasimhan, Mixed mode (I and II) crack tip fields in bulk metallic glasses, J. Mech. Phys. Solids 57 (2009) 1880–1897, doi:10.1016/j.jmps.2009.07.006.

[34] R.L. Narayan, P. Tandaiya, G.R. Garrett, M.D. Demetriou, U. Ramamurty, G. Garett, M.D. Demetriou, U. Ramamurty, On the variability in fracture toughness of 'ductile' bulk metallic glasses, Scr. Mater. 102 (2015) 75–78, doi:10.1016/j.scriptamat.2015.02.017.

[35] P. Tandaiya, U. Ramamurty, G. Ravichandran, R. Narasimhan, Effect of Poisson's ratio on crack tip fields and fracture behavior of metallic glasses, Acta Mater. 56 (2008) 6077–6086, doi:10.1016/j.actamat.2008.08.018.

[36] R.L. Narayan, P. Tandaiya, R. Narasimhan, U. Ramamurty, Wallner lines, crack velocity and mechanisms of crack nucleation and growth in a brittle bulk metallic glass, Acta Mater. (2014), doi:10.1016/j.actamat.2014.07.024.

[37] D. Raut, R.L. Narayan, P. Tandaiya, U. Ramamurty, Temperature-dependence of mode I fracture toughness of a bulk metallic glass, Acta Mater. 144 (2018) 325–336, doi:10.1016/j.actamat.2017.10.063.

[38] P. Tandaiya, R. Narasimhan, U. Ramamurty, Mode I crack tip fields in amorphous materials with application to metallic glasses, Acta Mater. 55 (2007) 6541–6552, doi:10.1016/j.actamat.2007.08.017.

[39] P. Tandaiya, R. Narasimhan, U. Ramamurty, On the mechanism and the length scales involved in the ductile fracture of a bulk metallic glass, Acta Mater. 61 (2013) 1558–1570, doi:10.1016/j.actamat.2012.11.033.

[40] G.N. Yang, Y. Shao, K.F. Yao, Understanding the fracture behaviors of metallic glasses-an overview, Appl. Sci. 9 (2019), doi:10.3390/app9204277.

[41] D. Raut, R.L. Narayan, Y. Yokoyama, P. Tandaiya, U. Ramamurty, Fracture of notched ductile bulk metallic glass bars subjected to tension-torsion: Experiments and simulations, Acta Mater. (2019), doi:10.1016/j.actamat.2019.02.025.

[42] W. Song, X. Meng, Y. Wu, D. Cao, H. Wang, X. Liu, X. Wang, Z. Lu, Improving plasticity of the Zr46Cu46Al8 bulk metallic glass via thermal rejuvenation, Sci. Bull. 63 (2018) 840–844, doi:10.1016/j.scib.2018.04.021.

[43] F. Szuecs, C.P. Kim, W.L. Johnson, Mechanical properties of Zr56.2Ti13.8Nb5.0Cu6.9Ni5.6Be12.5 ductile phase reinforced bulk metallic glass composite, Acta Mater. 49 (2001) 1507–1513, doi:10.1016/S1359-6454(01)00068-4.

[44] Y.S. Oh, C.P. Kim, S. Lee, N.J. Kim, Microstructure and tensile properties of high-strength high-ductility Ti-based amorphous matrix composites containing ductile dendrites, Acta Mater. 59 (2011) 7277–7286, doi:10.1016/j.actamat.2011.08.006.

[45] Y. Wu, Y. Xiao, G. Chen, C.T. Liu, Z. Lu, Bulk metallic glass composites with transformation-mediated work-hardening and ductility, Adv. Mater. 22 (2010) 2770–2773, doi:10.1002/adma.201000482.

[46] H. Zhai, H. Wang, F. Liu, A strategy for designing bulk metallic glass composites with excellent work-hardening and large tensile ductility, J. Alloys Compd. 685 (2016) 322–330, doi:10.1016/j.jallcom.2016.05.290.

[47] R.D.D. Conner, A.J.J. Rosakis, W.L.L. Johnson, D.M.M. Owen, Fracture toughness determination for a beryllium-bearing bulk metallic glass, Scr. Mater. 37 (1997) 1373–1378, doi:10.1016/S1359-6462(97)00250-9.

[48] C.J. Gilbert, R.O. Ritchie, W.L. Johnson, Fracture toughness and fatigue-crack propagation in a Zr–Ti–Ni–Cu–Be bulk metallic glass, Appl. Phys. Lett. 71 (1997) 476, doi:10.1063/1.119610.

[49] J. Schroers, W.L. Johnson, Ductile bulk metallic glass, Phys. Rev. Lett. 93 (2004) 255506, doi:10.1103/PhysRevLett.93.255506.

[50] R.L. Narayan, D. Raut, U. Ramamurty, A quantitative connection between shear band mediated plasticity and fracture initiation toughness of metallic glasses, Acta Mater. 150 (2018) 69–77, doi:10.1016/J.ACTAMAT.2018.03.011.

[51] L. Shao, J. Ketkaew, P. Gong, S. Zhao, S. Sohn, P. Bordeenithikasem, A. Datye, R.M.O. Mota, N. Liu, S.A. Kube, Y. Liu, W. Chen, K. Yao, S. Wu, J. Schroers, Effect of chemical composition on the fracture toughness of bulk metallic glasses, Materialia 12 (2020) 100828, doi:10.1016/j.mtla.2020.100828.

[52] J.R. Rice, P.C. Paris, J.G. Merkle, Some Further Results of J-Integral Analysis and Estimates, ASTM International, West Conshohocken, PA, 1973 978-0-8031-8151-9.

[53] T. Keiichiro, I. Hitoshi, Elastic-plastic fracture toughness test under mixed mode I-II loading, Eng. Fract. Mech. 41 (1992) 529–540, doi:10.1016/0013-7944(92)90299-T.

[54] K.V Vaishakh, R. Narasimhan, On the evaluation of energy release rate and mode mixity for ductile asymmetric four point bend specimens, Int. J. Fract. 217 (2019) 65–82, doi:10.1007/s10704-019-00369-7.

[55] S.V. Ketov, Y.H. Sun, S. Nachum, Z. Lu, A. Checchi, A.R. Beraldin, H.Y. Bai, W.H. Wang, D.V. Louzguine-Luzgin, M.A. Carpenter, A.L. Greer, Rejuvenation of metallic glasses by non-affine thermal strain, Nature 524 (2015) 200–203, doi:10.1038/nature14674.

[56] L. Zhang, S. Chen, H.M. Fu, H. Li, Z.W. Zhu, H.W. Zhang, Z.K. Li, A.M. Wang, H.F. Zhang, Tailoring modulus and hardness of in-situ formed β-Ti in bulk metallic glass composites by precipitation of isothermal ω-Ti, Mater. Des. 133 (2017) 82–90, doi:10.1016/j.matdes.2017.07.062.

[57] P.J. Bania, Beta titanium alloys and their role in the titanium industry, JOM 46 (1994) 16–19, doi:10.1007/BF03220742.

[58] I. Weiss, S.L. Semiatin, Thermomechanical processing of beta titanium alloys—an overview, Mater. Sci. Eng. A 243 (1998) 46–65, doi:10.1016/S0921-5093(97)00783-1.

[59] B. Gludovatz, D. Granata, K.V.S. Thurston, J.F. Löffler, R.O. Ritchie, On the understanding of the effects of sample size on the variability in fracture toughness of bulk metallic glasses, Acta Mater. 126 (2017) 494–506, doi:10.1016/j.actamat.2016.12.054.

[60] T.L. Anderson, Fracture Mechanics: Fundamentals and Applications, Taylor & Francis, 2012, doi:10.1016/j.jmps.2010.02.008.

[61] ASTM InternationalE1820-20b Standard Test Method for Measurement of Fracture Toughness, ASTM International, West Conshohocken, PA, 2020, doi:10.1520/E1820-20B.